Maintenance Mechanisms of Orographic Quasi-Stationary Convective Band Formed over the Eastern Part of Shikoku, Japan

Akira NISHII[1]

Institute for Space-Earth Environmental Research, Nagoya University, Nagoya, Japan

Graduate School of Environmental Studies, Nagoya University, Nagoya, Japan

Taro SHINODA

Institute for Space-Earth Environmental Research, Nagoya University, Nagoya, Japan

and

Koji SASSA

Faculty of Science and Technology, Kochi University, Kochi, Japan

June 18, 2024

----

1) Corresponding author: Akira NISHII, Institute for Space-Earth Environmental Research, Nagoya University, Furo-cho, Chikusa-ku, Nagoya 464-8601, Japan.
Email: nishii.akira@nagoya-u.jp

Abstract

This study examines the maintenance mechanisms of Muroto Lines (ML), a south-north oriented quasi-stationary convective band (QSCB) that appeared from the Muroto Peninsula in eastern Shikoku, Japan. The analysis area is characterized by complex orography, where many small-scale ridges are embedded in larger-scale ridges. We focused on two cases of ML that brought heavy rainfall: Case 1 (12-20 JST (Japan Standard Time; UTC+9 h) on July 3, 2018) and Case 2 (16-21 JST on August 15, 2018).

Atmospheric environments were characterized by warm-moist, and conditionally unstable lowest-level inflows (below 500 m in height) between east-southeasterly and south-southeasterly, and high humidity below the middle troposphere. The MLs exhibited back-building structures; convective cells were continuously generated at the southernmost tip of the MLs and advected northward by southerly wind 2-4 km in height. The convective cells in the MLs could be generated through two mechanisms: upslope lifting over a small-scale ridge oriented from south-southwest to north-northeast and convergence resulting from deflected flow at the ridge combined with undeflected flow at the eastern foot of the ridge. The former (latter) mechanism prevailed when the lowest-level wind direction was east-southeasterly (between southeasterly and south-southeasterly directions). Convergence at small-scale concave valleys and the lowest-level inflow with easterly components could further develop the ML. The vertical structures of the MLs showed that the heaviest rainfall in Case 1 (Case 2) was mainly due to relatively shallow (deep) convective cells, suggesting the importance of the collision-coalescence of raindrops (melting of graupel particles). Heavy rainfall in both cases was also caused by the development stage of convective cells by the collision-coalescence of raindrops in the southern part of the MLs. This study highlights the importance of orographic effects on the small-scale orography and cross-QSCB lowest-level inflow for the maintenance of heavy-rain-induced orographic QSCBs in warm and moist environments.

Keywords mesoscale convective system; localized heavy rainfall; quasi-stationary convective band; orographic precipitation

1. Introduction

The largest rainfall accumulation causes when the strongest rainfall occurs for the longest time (Doswell et al. 1996). Such rainfall can be caused by precipitation systems with a strong rainfall intensity and slow system motion. A quasi-stationary convective band (QSCB), which is a formation mode of line-shaped mesoscale convective systems (MCSs) that cause heavy rainfall in nearly the same area for longer than a few hours, has caused historical heavy rainfall events (e.g., Kawano and Kawamura 2020; Araki et al. 2021) because of its intense precipitation and high stationarity. Kato (2020) showed that half of the heavy rainfall events that occurred in Japan had line-shaped heavy rainfall areas (50–300 km in length and 20–50 km in width). To improve forecasting skills for heavy rainfall events, it is important to understand the factors behind the intense rainfall and stationarity of QSCBs.

Many previous studies have shown favorable atmospheric factors for the maintenance of QSCBs (e.g., Unuma and Takemi 2016a and b; Bluestein and Jain 1985; Kato 2020). Kato (2020) suggested the following six favorable environmental factors for diagnostic forecasts of QSCBs based on heavy rainfall events brought by them in Japan. However, Kato (2020) also noted that QSCBs do not always appear in areas where all the favorable conditions are met. Numerical studies (Kato and Aranami 2005; Kato 2020) have demonstrated that the representation of QSCBs is highly sensitive to low-level wind fields. Low- and mid-level wind directions are also important in determining the orientation of QSCBs (e.g., Yoshizaki et al. 2000; Morotomi et el. 2012; Oue et al. 2014). Further investigations into the atmospheric conditions of QSCBs that occur at various locations are required to identify the environmental factors for the maintenance of QSCBs.

The internal structure of QSCBs can vary with the vertical wind shear between the low and middle levels. Seko and Nakamura (2003) classified QSCBs into three types based on their internal structures: 1) squall line (SL) type, characterized by continuously generated cells along a stationary localized front; 2) back-building (BB) type, maintained by convective cells generated at the upstream side advected to the downstream side; and 3) back-and-side building (BSB) type, similar to BB-type QSCBs but with additional convective cells generated at the lateral side of the QSCBs. They showed that SL-, BB-, and BSB-type QSCBs appeared when the mid-level wind direction was opposite, the same, or perpendicular to the low-level wind direction, respectively. BB-type QSCBs frequently cause localized heavy rainfall events (e.g., Ogura 1990; Kato 2020; Schumacher and Johnson 2005). Schumacher and Johnson (2005) reported that BB-type MCSs in the U.S. are maintained by mesoscale and storm-scale processes (particularly storm-generated cold pools) rather than synoptic boundaries. However, cold pools can play a minor role in the BB-type QSCBs that occur in warm and moist environments (Kato 1998; Gascón et al., 2016; Kawano and Kawamura 2020). Instead of cold pools, other forcings such as orographic effects may be essential for maintaining QSCBs.

Orographic effects usually play an essential role in the maintenance of QSCBs formed over and near mountainous regions. However, specific orographic effects can vary according to various factors, such as the atmospheric environment and orographic shape. Houze (2012) categorized the orographic effects on precipitating clouds into six main types: upslope flow, diurnal forcing, pre-existing cloud passage over small terrain features, seeder-feeder mechanism, lee-side wave triggering, blocking effects, and capping effect. The upslope lifting of warm-moist airflow at mountain ranges is a typical maintenance mechanism of heavy orographic rainfall (e.g., Pontrelli et al., 1999; Morotomi et al. 2012). The blocked and deflected flow around large-scale mountain ranges (which may be larger than 100 km on a horizontal scale) can maintain QSCBs by forming low-level convergence with the undeflected flow from the ocean (Watanabe and Ogura, 1987; Yu and Hsieh 2009). Barrett et al. (2015) found that only three of 21 ensemble members reproduced the orographic QSCB formed in the central part of the U.K., and that the QSCB was reproduced when low-level wind flowed around the upstream mountain (50 km on a horizontal scale) and converged on its lee side. Small-scale orography (less than 20 km in horizontal spacing and 500-1500 m in height) can also play a key role in the maintenance and enhancement of orographic QSCBs, particularly in warm and moist environments where the LFC is very low (Gascón et al., 2016). Yoshizaki et al. (2000) found that upslope lifting over a ridge on the Nagasaki Peninsula (600 m maximum height and 20 km horizontal spacing) located on the north part of Kyushu Island in Japan triggered an orographic QSCB called the Nagasaki Line. Kato (2005) statistically revealed that the Nagasaki Line can be maintained during the Baiu season when the low-level wind direction is southwesterly and the wind speed at the

850 hPa level is between 5 and 25 m s^{-1}. Morotomi et al. (2012) suggested that convergence in a small-scale concave valley, opened in the direction of low-level south-southeasterly wind, contributed to the further development of QSCBs formed along the Ibuki-Suzuka Mountains (900 m maximum height and 20 km horizontal spacing) in central Japan. These studies suggest that orographic effects on contributed to the maintenance of QSCBs are highly sensitive to low-level wind fields. Because the orography usually has complex small-scale features, investigating the orographic features and low-level winds that contribute to the maintenance of orographic QSCBs occurred in various regions can enhance our understanding of their maintenance mechanisms.

The targets of the present study were two cases of south-north oriented QSCBs that brought localized heavy rainfall to nearly the same area in the eastern part of Shikoku, one Fig. 1 of the heaviest rainfall areas in Japan (~4500 mm yr^{-1}). We named these QSCBs the Muroto Lines (MLs) because they appeared on the Muroto Peninsula, located on the southeastern part of Shikoku (Fig. 1b). The first case (Case 1) brought heavy rainfall from 12 to 20 JST (Japan Standard Time; UTC +9) on July 3, 2018 (Fig. 1c). This case is characterized by two lines of heavy rainfall areas which has been caused by the shifting of the maintenance location. Case 2 experienced heavy rain from 16 to 21 JST on August 15, 2018 (Fig. 1d). In this case, ML maintained the same location during the event. The maximum accumulated rainfall in each case was very high (309 mm for 8 h in Case 1 and 422 mm for 5 h in Case 2), although the horizontal scales of the heavy rain area of the MLs (50 km in length and 10 km in width) were smaller than those of the QSCBs frequently focused on in Japan (e.g., Kato 2020; Hirockawa et al. 2022). Unuma and Murata (2012) statistically investigated the QSCBs that appeared over Shikoku and identified the ML when the wind direction at 850 hPa was southeasterly. Umemoto et al. (2005) analyzed the ML maintained for 20 h on July 31 and August 1, 2004, and concluded that upslope lifting at the orography in the Moroto Peninsula played a key role in maintaining the ML. However, the mechanisms that determine the maintenance locations of ML remain unclear.

This study focuses on the role of small-scale orography in the maintenance of the MLs, which has not been investigated in the previous studies but can play a key role in their maintenance. This focus is relevant because the analysis area is characterized by complex orography. The orography can be largely divided into two regions at 33.7°N (Fig. 1b): the west-east oriented Shikoku Main Ridge (maximum height of approximately 2000 m) and the south-north oriented main ridge (SN main ridge; the maximum height of approximately 1400 m). Many small-scale ridges with various orientations were embedded in both main ridges. For example, in the southernmost part of the Muroto Peninsula, a steep small-scale ridge (SR in Fig. 1b; 20 km long, 5 km wide, and 750 m high) oriented from south-southwest to north-northeast was embedded in the SN main ridge. The southern part of the SR ridge protrudes slightly to the east compared with its northern part. Some ridges formed small-scale concave valleys (e.g., CV1 and CV2 in Fig. 1b). Such small-scale orographic features may contribute to the maintenance of the ML because QSCBs bring localized heavy rainfall events that are usually maintained by mesoscale and storm-scale (O(10 km) for the ML) processes (Schumacher and Johnson 2005).

The vertical structure of the ML differs between the two cases. Figure 2 shows snapshots Fig. 2 of the radar horizontal reflectivity (Z_h) at a height of 2 km and vertical cross sections along the MLs observed by the Japan Meteorological Agency (JMA) Murotomisaki radar. Although the horizontal distribution of Z_h was almost identical in both cases (Figs. 2a and 2c), the echo-top height in Case 2 was higher than that in Case 1 (Figs. 2b and 2d). Recent studies (e.g., Hamada et al. 2015; Hamada and Takayabu 2018; Sohn et al. 2013) have shown that heavy rainfall can also be produced by relatively shallow convective cells through the collision and coalescence of raindrops (warm-rain processes), which differs from the generally accepted heavy-rain-producing processes where the melting of graupel particles in deep convective clouds produces intense rainfall (cold-rain processes). The present study also documents the differences in the vertical Z_h structures between the two cases, which can help understand the heavy-rain-producing processes of orographic QSCBs.

The purpose of this study was to clarify the maintenance mechanisms of the two cases of ML and document the differences in their vertical structures. Section 2 describes the data and methods used in this study. Section 3 provides an overview of the two cases. Sections 4 and 5 present the results and discussions, respectively. Section 6 summarizes the present study.

2. Data and Method

To analyze the horizontal structures of the MLs, we used Extended RAdar Information Network (XRAIN) composited rainfall intensity data provided by the Ministry of Land, Infrastructure, Transport, and Tourism (MLIT) in Japan. This dataset comprises rainfall intensity at a height of approximately 2 km estimated from Z_h and the specific differential phase (K_{dp}) collected by MLIT C- and X-band weather radars (mostly dual-polarized) installed across Japan. The horizontal and temporal resolutions of the dataset are 250 m and 1 min, respectively. We note that unrealistic rainfall intensity sometimes appears within 10 km of one of the XRAIN C-band polarimetric radars located in the northern part of the ML in Case 1 (33.89°N, 134.24°E; a yellow triangle in Fig. 1c).

We also utilized the Plan Position Indicator (PPI) data of Z_h observed using the C-band single-polarimetric JMA Murotomisaki radar located at the southernmost tip of the Muroto Peninsula (blue triangle in Fig.1c) to investigate the vertical structures of the MLs. Note that this radar is not part of XRAIN. We used 12 elevation angles of PPIs ranging from 0.4° to 25.0°, observed every 10 min. We manually excluded beam blockage areas that appeared at the lower elevation angles of the PPIs (0.4°, 1.2°, and 1.9°). Z_h were corrected for rainfall attenuation with a relation $A = \int_0^r 2\, K(r)\, dr$; where A is total rainfall attenuation along a beam path, r is a distance from the radar, K represents one-way specific attenuation defined by $K = 0.0018\ R^{1.05}$ (Doviak and Zrnić 1992), R is rainfall intensity estimated from Z_h (mm^6 m^{-3}) using the relationship $Z_h = 200\ R^{1.6}$. The PPI data were interpolated to constant altitude plan position indicator (CAPPI) grids using the method of Cressman (1959) with a horizontal resolution of 1 km and a vertical resolution of 0.5 km. We conducted echo-top height and contour frequency altitude of the diagram (CFAD, Yuter and Hauze 1995) analyses using CAPPI data. To capture the vertical structure of heavy rainfall areas, a CFAD analysis was conducted on vertical columns where Z_h was 35 dBZ or greater at a height of 1.5 km. Z_h was binned every 1 dBZ in the range 5–60 dBZ. The frequencies in the CFADs were normalized to the maximum absolute frequency in each diagram to facilitate vertical comparisons (Houze et al. 2007).

We analyzed the atmospheric conditions of the MLs using observational and reanalysis data. Data from the JMA Automated Meteorological Data Acquisition System (AMeDAS) at Murotomisaki (blue triangle in Fig.1c, the same location as the JMA Murotomisaki radar) and Kaiyo (red square in Fig. 1c) were used to analyze the atmospheric environment near the surface. The observation heights at Murotomisaki and Kaiyo were 185 m and 5 m, respectively. We used local pressure, temperature, RH, and wind data from Murotomisaki and temperature data from Kaiyo at 10 min intervals. Vertical profiles of the 10 min averaged horizontal wind collected by the JMA wind profiler radar located in Kochi (green circle in Fig. 1c) were also used. We excluded data above 6 km in height owing to the high frequency of missing values. To analyze the thermodynamic environment, we used the initial value of the JMA Mesoscale model (JMA-MSM), provided every 3 hours. This dataset contained geopotential height, temperature, horizontal wind, and RH with a horizontal resolution of

0.125° (zonal) × 0.1° (meridional) and 16 pressure levels (10 levels for RH). The JMA surface weather charts were used to determine the synoptic environment.

3. Cases overview

Figure 3 shows the horizontal distribution of hourly rainfall during Case 1 derived from the XRAIN rainfall intensity. A Line-shaped heavy rain area, where the hourly rainfall was 20 mm h^{-1} or greater with maximum rainfall exceeding 50 mm h^{-1} brought by the ML, appeared between 12 and 20 JST on July 3, 2018. We primarily focused on the period when such line-shaped heavy-rain areas appeared. The ML persisted in almost the same area from 12 to 15 JST, then gradually shifted eastward between 15 and 17 JST, and was maintained 5 km to the east after 17 JST. This shift resulted in the appearance of two lines of accumulated rainfall (Fig. 1c). We further divided Case 1 into Case 1A (12-15 JST) and Case 1B (17-20 JST) to compare the maintenance mechanisms between the two periods. The ML persisted until approximately 00 JST on July 4; however, its intensity was weak (not shown). Fig. 3

In Case 2, ML caused heavy rainfall from 16 to 21 JST on August 15, 2018 (Fig. 4). The ML persisted at almost the same location for 5 hours. The maximum hourly rainfall (127 mm, 19-20 JST) in Case 2 was slightly higher than that of Case 1 (107 mm, 16-17 JST). The ML occasionally appeared until 00 JST on August 16 but did not persist for longer than an hour (not shown). Fig. 4

4. Results

4.1 Atmospheric environments

Figures 5a and 5b show the JMA surface weather charts analyzed just before the two cases. In Case 1 (Fig. 5a), Typhoon Prapiroon was located 600 km west of the ML, and the North Pacific High existed to the east at 09 JST on July 3, 2018. The typhoon moved northeast at a speed of 25 km h^{-1} and reached east of Tsushima Island at 21 JST on July 3 (not shown). The synoptic environment in Case 2 (Fig. 5b) was similar to that in Case 1, as characterized by two tropical cyclones (a tropical depression (TD in Fig. 5b) and Typhoon Rumbia) to the west and the North Pacific High to the east of Shikoku. Fig. 5

Figures 5c and 5d show the horizontal distributions of the equivalent potential temperature (EPT: calculated with a method of Bolton (1980)) and horizontal wind at the 950 hPa level, and geopotential height at the 500 hPa level derived from the initial value of the JMA-MSM at the same time as Figs. 5a and 5b, respectively. In Case 1, a warm-moist southeasterly airflow with an EPT higher than 345 K intruded the analysis area at 950 hPa. Such a warm-moist airflow also flowed into the area from south-southeast in Case 2. The 5880 m contour line of the geopotential height at the 500 hPa level in Case 2 extended farther east than in Case 1, indicating that the North Pacific High was stronger in Case 2. The absence of an upper-level trough near Shikoku (Figs. 5c and 5d) and the distant location (800 km north of Shikoku) of the stationary fronts (Figs. 5a and 5b) suggest that synoptic forced convergence should not play a direct role in the maintenance of the MLs.

Figure 6 shows the skew-T log-p diagrams of temperature and dew-point temperature (Fig. 6a) and vertical profiles of RH (Fig. 6b) at 12 JST on July 3, 2018 (Case 1, solid lines) and at 15 JST on August 15, 2018 (Case 2, dashed lines). Each profile is the mean value averaged within a red dashed rectangle (3 × 3 grid), as shown in the lower-left map of Fig. 6a, corresponding to the upstream side of the low-level wind of the ML in both cases. The vertical temperature profiles in both cases indicate a conditionally unstable environment. The convective available potential energy (CAPE), convective inhibition (CIN), lifted condensation level (LCL), LFC, and LNB in Case 1 (Case 2), averaged over the same areas as the profiles in Fig. 6, were 803 J kg^{-1} (2096 J kg^{-1}), 0.0 J kg^{-1} (0.2 J kg^{-1}), 504 m (554 m), 640 m (1033 m), and 11450 m (14770 m), respectively. The lower LFC and almost zero CIN values suggest that convective cells can be easily triggered by upslope lifting over small-scale ridges on the Muroto Peninsula (Fig. 1b). The higher values of CAPE and LNB in Case 2 indicate that the atmospheric conditions were more favorable for deeper convection than in Case 1, which is consistent with the vertical cross-sections of the MLs (Fig. 2). The RH (Fig. 6b) exceeded 80% below the 600 hPa level in both cases, indicating a moist environment below the middle troposphere. Fig. 6

Figure 7 shows the time series of the AMeDAS observations at Murotomisaki and Kaiyo (only shown at the potential temperature). The potential temperature was displayed because the observation heights of the two sites differed by 180 m. In Case 1, the surface wind speed was maintained between 12 and 15 m s^{-1} (Fig. 7a). The wind speed of Case 2 (Fig. 7f) was Fig.7

weaker (5–9 m s^{-1}) than that of Case 1. The surface wind direction in Case 1 (Fig. 7b) gradually shifted from east-southeasterly at 12 JST to south-southeasterly at 20 JST. The ML brought heavy rainfall when the wind direction was between south-southeasterly and east-southeasterly. From 14:10 to 17:10 JST, the wind direction changed from east-southeasterly to south-southeasterly, almost coinciding with the transition from Case 1A to Case 1B. This suggests that the transition in the maintenance location of the ML could be linked to veering of the surface wind direction. Case 2 brought heavy rainfall when the wind direction ranged between south-southeasterly and southeasterly (Fig. 7g). The amount of surface WVF (defined by WVF = $\rho\ q_v\ u$, where ρ is air density, q_v is water vapor mixing ratio, and u is wind speed) was higher (250-350 g m^{-2} s^{-1} in Case 1 and 190-250 g m^{-2} s^{-1} in Case 2) than the value of favorable atmospheric conditions for QSCBs presented by Kato (2020) (> 150 g m^{-2} s^{-1}) in both cases, indicating the rich intrusion of water vapor to the ML. The temporal changes in the amount of WVF were explained by the wind speed in both cases, as the water–vapor mixing ratio remained almost constant (Figs. 7c and 7h). The potential temperatures at Murotomisaki and Kaiyo (solid and dashed lines in Figs. 7e and 7j, respectively) showed that the differences between the two sites were within 2 K, and no steep temperature drop was observed at Kaiyo (5 km east of the ML). This implies that the strong cold outflow from the ML could not reach Kaiyo.

Figure 8 shows hodographs of the mean horizontal wind below a height of 6 km obtained by the wind profiler radar at Kochi and the AMeDAS at Murotomisaki during each period. All

Fig. 8

cases were characterized by veering features in the wind direction. The values of SREH (calculated from the surface to 3 km in height and cell-motion speed was estimated with a method of Bunkers et al. (2000)) during Case 1A, 1B, and 2 were 213.7 m^2 s^{-2}, 194.5 m^2 s^{-2}, and 83.0 m^2 s^{-2}, respectively, suggesting the existence of strong vertical wind shear. The orientations of the ML, obtained by averaging those of the heavy rain areas (Figs. 3 and 4), almost corresponded to the direction of the southerly wind between 2 and 4 km in height in all periods. From Cases 1A to 1B (Fig. 8a and b), the lowest-level wind direction (below 500 m in height) changed from east-southeasterly and southeasterly to south-southeasterly. The vertical profile of the horizontal wind direction in Case 2 (Fig. 8c) was similar to that in Case 1B; however, the wind speed in Case 2 was half of that in Case 1B below 6 km in height.

4.2 Horizontal structures of the MLs

Figure 9 shows a time-latitude section of XRAIN maximum rainfall intensity between 134.1°E and 134.4°E during Case 1. Maximum rainfall intensity frequently reached stronger than 120 mm h^{-1} between 33.65°N and 33.80°N, and occasionally exceeded 150 mm h^{-1}. Many lines of strong rainfall intensity extending diagonally up to the right appeared in this case. This indicates that convective cells were generated in the southernmost part of the ML (mostly between 33.4°N and 33.5°N) and moved northward, suggesting that the ML in Case 1 was a BB type QSCB. The meridional moving speed of convective cells estimated from the orientation of lines of heavy rainfall was between 20 and 25 m s^{-1}, almost corresponding

Fig. 9

to the southerly component of wind speed at approximately 2–4 km in height (Figs. 8a and 8b). The southernmost tip of the heavy rainfall intensity (greater than 20 mm h^{-1}) shifted approximately 5 km north after 17 JST.

Figure 10 shows the time-latitude section of XRAIN maximum rainfall intensity between 134.15°E and 134.45°E during Case 2. Maximum rainfall intensity usually exceeded 120 mm h^{-1} between 33.55°N and 33.75°N. Convective cells were continuously generated until 20 JST from 33.4°N and moved northward at a speed of approximately 12 m s^{-1}. This suggests that the ML in Case 2 was a BB-type QSCB, similar to Case 1. The meridional moving speed (approximately 12 m s^{-1}) corresponded to the meridional component of wind speeds higher than 2 km in height (Fig. 8c). Fig. 10

Figure 11 shows longitude-time cross sections of XRAIN rainfall intensity around the southernmost part of the ML. In Case 1 (Fig. 11a), convective cells of the ML passed around 134.18°E until 15 JST (i.e., during Case 1A). The locations of convective cells gradually shifted to the east after 15 JST and maintained around 134.22°E after 17 JST. In Case 1B, weak convective cells repeatedly appeared at the location where Case 1A was maintained, indicating the existence of a weak band. A similar weak band persisted in Case 2, 5 km west of the ML (Fig. 11b). This indicates that two convective bands were simultaneously maintained during Cases 1B and 2, and that the band that appeared on the upward (i.e., eastern) side of the low-level wind developed into the ML. Fig. 11

The comparison of mean XRAIN rainfall intensity with the orography (Fig. 12) during each period suggests that convective cells of the MLs were not always generated over ridges located beneath the southernmost part of the MLs. In Case 1A (Fig. 12a), the ML was maintained over the SN Main Ridge, and the southernmost tip of the ML (mean rainfall intensity greater than 1 mm h^{-1}) was located over the SR (Fig. 12b). The ML brought the heaviest rainfall around 33.72°N, 133.21°E, where relatively high orography (higher than 1000 m in height) was located. A small peak in the mean rainfall intensity greater than 30 mm h^{-1} was also found around 33.5°N, just north of the CV1. During Case 1B (Fig. 12c), the ML was maintained 5 km east of Case 1A. The southernmost tip of the ML shifts toward the eastern foot of the SR (Fig 12d). The orography beneath the southern part of ML is generally lower than 500 m in height. The heaviest rainfall area (a contour higher than 50 mm h^{-1}) appeared around the southernmost slope of the Shikoku Main Ridge. A small peak in mean rainfall intensity appeared just north of the CV2. The weak band shown in Fig.11a is located west of the ML. In Case 2, the ML was maintained at almost the same location as that in Case 1B, and its southernmost tip was located over the eastern foot of the SR (Fig. 12f). The contour of 1 mm h^{-1} bulged to the west between 33.4°N and 33.55°N indicates the weak band shown in Fig. 11b. The results in Fig. 12 suggest that upslope lifting over ridge slopes can contribute to the maintenance of the ML in Case 1A. However, orographic effects other than upslope lifting could also have played a significant role in maintaining the ML during

Fig. 12

Cases 1B and 2, in which the southernmost part of the ML appeared at the eastern foot of the SR.

4.3 Vertical structures of the MLs

Figure 13 displays the appearance frequencies of the longitudinal maximum echo-top height obtained from the JMA Murotomisaki radar; the longitudinal maximum values of the mean rainfall intensity in the areas are indicated by red-dotted rectangles in Fig. 12 for each period. We analyzed the echo-top heights of 15 and 35 dBZ to capture the maximum height of rain and snow and the existence of heavy rain and graupel, respectively. In all periods, a high frequency (> 30%) appeared at each latitude, indicating that the developmental stages of each convective cell at a certain latitude were generally the same. This allowed us to statistically capture the general characteristics of the vertical structures of ML at that latitude. During Case 1A, the 15 dBZ echo-top height (Fig. 13a) was mostly lower than 9 km in height and most of the 35 dBZ echo-top height (Fig. 13b) did not exceed -10 °C level. This suggests that graupel particles were mostly absent in Case 1A. The highest value of maximum mean rainfall intensity appeared at 33.72°N, where a high 15 dBZ echo-top height (9 km) frequently observed, suggesting that the mature stage of convective cells brought the heaviest rainfall. A small peak also appeared at 33.49°N, corresponding to the small peak of mean rainfall intensity found in Fig. 12b. The peak appearing at 33.84°N is doubtful because it is located near the XRAIN C-band radar, where

Fig. 13

erroneous data frequently appear, as described in Section 2. The echo-top height in Case 1B (Fig. 13c and d) had characteristics similar to those of Case 1A. The differences can be found between 33.73°N and 33.76°N, where maximum mean rainfall intensity rapidly increased at the south of its highest value. The location of this rapid increase corresponds to the southern slope of the Shikoku Main Ridge, implying that upslope lifting further developed the ML. In Case 2, the 15 dBZ echo-top height exceeded 16 km at a maximum (Fig. 13e) and high appearance frequency of 35 dBZ echo-top height usually reached higher than -10 °C level (Fig. 13f), suggesting the existence of graupel particles. The location of the highest mean maximum rainfall intensity and the highest 15 dBZ echo-top height matched, indicating that the heaviest rainfall occurred at the mature stage of the convective cells. Mean maximum rainfall intensity greater than 20 mm h^{-1} appeared at the early development stage of convective cells where the peak appearance frequency of 15 dBZ echo-top height existed around 0 °C level (around 33.5°N).

Figure 14 shows the two cases (Case 1 B and Case 2) of normalized CFADs analyzed Fig. 14
over the areas indicated by black dashed rectangles in Fig. 12: the southernmost part of the heavy rainfall area (mean rainfall intensity of 20 mm^{-1} or greater) and the heaviest rainfall area. The number of samples collected at each height is shown in the right panel of each CFAD. Case 1A was excluded from the CFAD analysis because of the appearance of severe beam blockage at the maintenance location. In the heaviest rainfall area of Case 1B (Fig. 14a), the value of median Z_h was 15 dBZ at the -10 °C level (6.7 km in height) and

rapidly increased to 29 dBZ at the 0 °C (4.8 km in height), then reached 40 dBZ at 1.5 km in height. This suggests that Z_h growth below the 0 °C level (i.e., collision and coalescence of raindrops) was essential for producing heavy rainfall in Case 1B. In the heaviest rainfall area of Case 2 (Fig. 14c), the median values of Z_h at -10 °C level, 0 °C (5.2 km in height), and at 1.5 km in height was 30 dBZ, 37 dBZ, and 44 dBZ, respectively. The number of samples collected at each height (right panel of Fig. 12c) was almost constant below 12 km. Compared with Case 1B, the vertical structure of Case 2 was characterized by a high Z_h above the 0 °C level and a lower Z_h growth below that level. These results suggest that graupel particles should exist above the 0 °C level and melting of them can be a primary factor on the production of the heaviest rainfall in Case 2.

The vertical Z_h structure between the two cases in the southernmost part of the heavy rainfall area (Fig. 14b and 14d) differed from that in the heaviest rainfall area, particularly in Case 2. In Case 1B (Fig. 14b), the vertical profile of median value of Z_h was similar (15 dBZ at the -10 °C level, 26 dBZ at the 0 °C level, and 40 dBZ at 1.5 km in height) to that in the heaviest rainfall area. While the number of samples (the right panel of Fig. 14b) rapidly decreased above the 0 °C level, indicating that heavy rain at the southernmost part of heavy rainfall area brought by shallower rainfall than that of the heaviest rainfall area in Case 1B. In Case 2 (Fig. 14d), the median values of Z_h above 0 °C was lower than that in the heaviest rainfall area (22 dBZ at the -10 °C level and 31 dBZ at 0 °C) but increased to 43 dBZ at 1.5 km in height. Such a lower Z_h above the 0 °C level and a large Z_h growth below that level resemble those observed in Case 1B. These results suggest that the collision and coalescence of raindrops played key roles in producing heavy rainfall in the southernmost part of the heavy rainfall area, where convective cells were developing.

5. Discussion

5.1 Maintenance mechanisms of the MLs

In both cases, the MLs suggested BB-type QSCBs with a line-shaped structure sustained through successive generation of convective cells in the southernmost part of the ML and their northward advection. The atmospheric environment factors affecting the maintenance of the ML were as follows: (1) intrusion of warm-moist air with a high EPT (greater than 345 K) from east-southeast and south-southeast at the lowest level. The inflow was conditionally unstable with almost zero CIN, a moderate to high CAPE value (803 J kg^{-1} in Case 1 and 2096 J kg^{-1} in Case 2), an LFC of approximately 1000 m or lower, and a large amount of WVF. Such an airflow can easily trigger convective cells if weak forcing (i.e., orographic forcing) exists. (2) Southerly wind at 2-4 km in height. Convective cells were advected northward by the middle-level winds. This southerly wind formed a strong vertical wind shear with low-level winds, which were essential for forming QSCBs (e.g., Unuma and Takemi 2016b; Bluestein and Jain 1985; LeMone et al 1998). (3) Very high humidity (RH > 80%) below 0 °C level (Fig. 6). This can suppress the evaporative cooling of raindrops and lead to weak storm-generated cold pools from the ML, which are usually important for the maintenance of BB-type QSCBs (Schumacher and Johnson 2005). The absence of a strong cold pool is evident from the lack of a steep temperature decrease beneath the ML (Figs. 7e and 7j). As the MLs were maintained over mountainous areas without synoptic low-level convergence (Fig. 5), orography should have played an essential role in their maintenance instead of the cold pool. The stationarity of the ML also suggests a weak cold pool. This is because, if a strong cold pool exists, convective cells can be generated east of the ML, where the strong cold pool and low-level inflow converge. The atmospheric conditions, excluding synoptic ascent (which was impossible to obtain from the data used in this study), met the favorable conditions suggested by Kato (2020), except for the SREH in Case 2 (83 $m^2\ s^{-2}$). However, the veering wind structure enabled the maintenance of the BB mechanism.

Umemoto et al. (2005) suggested that convective cells of the ML were repeatedly generated by upslope lifting over mountains on the Muroto Peninsula. However, upslope lifting alone could not explain the cell generation mechanisms in Cases 1B and 2, where precipitation occurred at the eastern foot of the SR (Fig. 12). To address this issue, we calculated the unsaturated moist Froude number (Fr_w) for the SR which defined by $Fr_w = U / (N_w H)$; where H is the representative height of SR (750 m, corresponding to the maximum height of the SR), U is the mean horizontal speed below H obtained from Fig. 8, N_w is the unsaturated moist Brunt–Väisälä frequency defined by $N_w^2 = (g/\overline{\theta}_v)(d\theta_v/dz)$ (Emanuel 1994), where $\overline{\theta}_v$ (calculated from Fig. 6) is the mean virtual potential temperature below H, g is the acceleration of gravity, and $d\theta_v/dz$ is calculated by θ_v at H and the surface. The Fr_w values for Cases 1A, 1B, and 2 were 2.40, 2.61, and 1.25, respectively. For an idealized situation, Fr_w greater than unity indicates that the flow passes over the mountain (e.g., Smith 1989; Smith 2019). This suggests that upslope lifting at the SR contributes to the formation of the southernmost convective cells in the ML, which cannot explain the eastern foot maintenance during Cases 1B and 2.

Instead of Fr_w, the relationship between the orientation of the SR and the lowest-level wind direction may explain the maintenance mechanisms of the ML. In Case 1A, the lowest-level wind was east-southeasterly (Fig. 8a), almost perpendicular to the SR orientation (from south–southwest to north-northeast). In contrast, the wind directions in Cases 1B and 2 were maintained when the lowest-level wind direction was southeasterly or south-southeasterly (Figs. 8b and 8c). The angle between the wind direction and the orientation of the SR in Case 1B was smaller than that in Case 1A. In a three-dimensional ridge, a flow with a lower angle of incidence tends to disperse to both sides of the ridge because it impinges on the narrower side of the ridge (Smith 1989). In addition, partial flow splitting, in which both upslope lifting and flow splitting occur simultaneously, has been reported in numerical simulations for both ideal (Smolarkiewicz and Rotunno 1989) and real orography (Yu et al. 2022) even when $Fr > 1$ (i.e., $Fr_w > 1$). Considering the lower angle of incidence of the lowest-level wind and the appearance of the weak band over the SR (Figs. 11, 12d, and 12f), partial flow splitting could have occurred during Cases 1B and 2 at the southern slope of the SR. When this occurred, two bands could be formed: the first was formed by upslope lifting, and the second was generated by low-level convergence at the eastern foot of the SR, which could be created by the split flow deflected to the south-southwesterly and undeflected southeasterly or south-southeasterly flow. In this case, the band formed at the eastern foot of the ridge (i.e., the ML) could have developed because this band was formed on the upstream side of the warm-moist lowest-level wind intruding from southeasterly and south-southeasterly. However, the band formed over the ridge could not develop further because the ML disrupted the supply of low-level water vapor, resulting in the formation of a weak band (Fig. 11).

The MLs could be further developed by acquiring water vapor from the lateral side of the ML because the low-level wind direction was not parallel to the orientation of the ML. Seko and Nakamura (2003) showed that a cross-QSCB low-level flow can form a BSB-type QSCB. However, the weak cold pool of the ML can create unfavorable conditions for the lateral triggering of convective cells, resulting in the formation of a BB-type ML. The importance of lateral inflow is also suggested by the weakening of the ML after 20 JST in Case 1 (Fig. 3), despite the increase in WVF (Fig. 7d). This weakening may have occurred because of a decrease in the eastern component of the low-level wind (Fig. 7b), resulting in a reduction in the lateral intrusion of water vapor.

Small-scale orographic features beneath ML may contribute to further development. In Case 1A (Case 1B), the mean rainfall intensity had a small peak immediately north of CV1 (CV2) (Fig. 12b and 12d). CV1 and CV2 are concave valleys opened on the east-southeast side and the south-southeast sides, respectively, and correspond to the low-level wind direction for each case. These situations favor the convergence of low-level water vapor in concave valleys (Morotomi et al. 2012; Yu et al. 2022) and resulting in a sufficient supply of water vapor to the ML.

This study suggests that orographic effects on small-scale topography beneath and near the ML and the lateral intrusion of low-level water vapor play key roles in ML maintenance. These factors could prevail under warm-moist environment, which is unfavorable for the formation of a strong cold pool.

5.2 Vertical structures and heavy-rain-producing processes of the ML

The vertical structures of Z_h (Figs. 13 and 14) indicate that convective cells of the ML in Case 1 were relatively shallow with a 15 dBZ echo-top height mostly below 9 km (Fig. 13a), whereas those in Case 2 were characterized by deep convections whose 15 dBZ echo top-height was higher than 16 km at maximum (Fig 13c). These differences can be attributed to differences in atmospheric instability. The atmospheric environment in Case 1 was characterized by relatively low CAPE and LNB (803 J kg^{-1} and 11450 m, respectively) and high RH (> 80%) below the middle level, featuring a relatively stable and humid environment that is not favorable for deep moist convection. These characteristics are comparable to those of the Baiu (Meiyu) season in East Asia (Zhang et al. 2006), where heavy rainfall with relatively shallow convection is frequently observed (e.g., Zhang et al. 2006; Oue et al. 2010; Oue et al. 2011). In contrast, the CAPE and LNB values were high (2096 J kg^{-1} and 14770 m, respectively) in Case 2, corresponding to the atmospheric conditions of deep convective heavy rainfall (e.g., Bluestein and Jain 1985; Araki et al. 2021). The tendencies of the echo-top heights in Cases 1A and 1B were almost the same, suggesting that the differences in the vertical structures between the two periods were small.

The CFADs at the heaviest rainfall area in the two cases (Figs. 14a and 14c) suggests that the heaviest rainfall in Case 1B were produced by collision and coalescence of raindrops below the 0 °C level, while those in Case 2 were primarily brought by the melting of graupel particles. In Case 1B (Fig. 14a), the vertical profile of the median of Z_h was characterized by the large decreasing rate of Z_h above the 0 °C level (7.4 dBZ km^{-1} from the 0 °C to the -10 °C level) and lower appearance height of the peak value. These features correspond to the vertical profile of Z_h in the convection of medium depths described by Zhang et al. (2006), which are relatively shallow convective cells (echo-top height of 15 dBZ is 8 km or lower) frequently observed during the Baiu (Meiyu) season. In the convection at medium depths, the collision and coalescence of raindrops is usually a key factor in the production of heavy rainfall (Oue et al. 2010; Oue et al. 2011). The large increment of Z_h below that level (from 29 dB at the 0 °C level to 40 dBZ at 1.5 km in height in median Z_h) in Fig. 14a suggests that collision and coalescence of raindrops was also the primary factor in the formation of the heaviest rainfall in Case 1B. A relatively stable and very humid environment and thick warm cloud layer (depth from LCL to the 0 °C level; 3.8 km) in Case 1B also indicated a high efficiency for the collision and coalescence processes, because raindrops could remain for a long time below the 0 °C layer without evaporation. In Case 2 (Fig. 14c), the median value of Z_h at the 0 °C level was very high (37 dBZ) and reached 30 dBZ even at the -10 °C level, inferring the existence of sufficient number of graupel particles.

Although Z_h increased below the 0 °C level, it suggests the occurrence of collision and coalescence of raindrops, with the magnitude of increment (7 dBZ from the 0 °C to 1.5 km in height in median values) being smaller than that in Case 1B (11 dBZ). This suggests that the melting of graupel particles was the primary factor producing the heaviest rainfall in Case 2, which is typical of heavy deep convective rainfall. The unstable environment of Case 2 could have led to an efficient growth of graupel particles above the 0 °C level, as strong updraft supplied a sufficient value of supercooled droplets and formed a favorable condition in the occurrence of riming process.

Strong rainfall also occurred during the developmental stage of convective cells in both cases. This is different from the atypical scheme of convective cells in which heavy rainfall is caused by the mature stage of convective storms (Byers and Braham 1949). The high growth rate of Z_h below 0 C° level observed in both cases (Fig. 14b and 14d), indicated that collision and coalescence of raindrops were dominant regardless of the atmospheric instability. The valley convergence formed at CV2 may have contributed to the promotion of warm rain processes by supplying a large amount of water vapor to convective cells.

6. Summary

This study examines the maintenance mechanisms of ML, a south-north oriented QSCB that appeared from the Muroto Peninsula in eastern Shikoku, Japan. The analysis area is characterized by complex orography, where many small-scale ridges are embedded in larger-scale ridges. We focused on two cases of ML that brought heavy rainfall: Case 1 (12-20 JST on July 3, 2018) and Case 2 (16-21 JST on August 15, 2018).

Atmospheric environments were characterized by warm-moist, and conditionally unstable lowest-level inflows (below 500 m in height) between east-southeasterly and south-southeasterly, and high humidity below the middle troposphere. The MLs exhibited back-building structures; convective cells were continuously generated at the southernmost tip of the MLs and advected northward by southerly wind 2-4 km in height. The convective cells in the MLs could be generated through two mechanisms: upslope lifting over a small-scale ridge oriented from south-southwest to north-northeast and convergence resulting from deflected flow at the ridge combined with undeflected flow at the eastern foot of the ridge. The former (latter) mechanism prevailed when the lowest-level wind direction was east-southeasterly (between southeasterly and south-southeasterly directions). Convergence at small-scale concave valleys and the lowest-level inflow with easterly components could further develop the ML. The vertical structures of the MLs showed that the heaviest rainfall in Case 1 (Case 2) was mainly due to relatively shallow (deep) convective cells, suggesting the importance of the collision-coalescence of raindrops (melting of graupel particles).

Heavy rainfall in both cases was also caused by the development stage of convective cells by the collision-coalescence of raindrops in the southern part of the MLs. This study highlights the importance of orographic effects on the small-scale orography and cross-QSCB lowest-level inflow for the maintenance of heavy-rain-induced orographic QSCBs in warm and moist environments.

To clarify the details of the wind field modulated by small-scale orography and cell-generating processes, numerical simulations with a horizontal resolution of 500 m or finer can be effective, as the horizontal scale of the small-scale orography focused on in this study was approximately 10 km. Furthermore, investigating the atmospheric environment and structures of other heavy-rain-producing MLs can reveal the common conditions for the appearance of ML and the relationship between the atmospheric environment and the depth of convective cells.

Data Availability Statement

XRAIN composite rainfall intensity data is available at the Data Integration and Analysis System (DIAS) operated by the Ministry of Education, Culture, Sports, Science and Technology of Japan (http://apps.diasjp.net/xband/). The initial value of JMA-MSM and the wind profiler radar data were provided by JMA and available from a data server operated by Research Institute for Sustainable Humanosphere (RISH), Kyoto University (http://database.rish.kyoto-u.ac.jp/index-e.html). AMeDAS data can be obtained at JMA website (https://www.data.jma.go.jp/stats/etrn/index.php). Digital Elevation Map provided by Geospatial Information Authority of Japan (https://fgd.gsi.go.jp/download/) (except for Fig. 1a) and National Aeronautics and Space Administration (NASA) Shuttle Radar Topography Mission (SRTM) 3 arc-seconds data (https://urs.earthdata.nasa.gov/) (for Fig. 1a) were used to display orography. Matplotlib (https://matplotlib.org) and Cartopy (https://scitools.org.uk/cartopy) were used for drawing figures. JMA Murotomisaki radar data is available from Japan Meteorological Business Support Center.

Acknowledgments

The authors appreciate to Mr. M. Kato for the supporting of analyzing the JMA Murotomisaki radar data and Prof. K. Tsuboki, Dr. S. Kanada, and other members of the Laboratory of Meteorology, Institute for Space-Earth Environmental Research in Nagoya University for their fruitful comments. This work was performed using the facilities of the Institute for Space-Earth Environmental Research, Nagoya University. The work was also supported by “formation of a virtual laboratory for diagnosing the earth’s climate system (VL)” defrayed by the MEXT, Japan.

References

Araki, K., T. Kato, Y. Hirockawa, and W. Mashiko, 2021: Characteristics of atmospheric environments of quasi-stationary convective bands in Kyushu, Japan during the July 2020 Heavy Rainfall Event. *SOLA*, **17**, 8-15.

Barrett, A. I., S. L. Gray, D. J. Kirshbaum, N. M. Roberts, D. M. Schultz, and J. G. Fairman Jr., 2015: Synoptic versus orographic control on stationary convective banding. *Quart. J. Roy. Meteor. Soc.*, **141**, 1101-1113.

Bluestein, H. B., and M. H. Jain, 1985: Formation of mesoscale lines of precipitation: Severe squall lines in Oklahoma during the Spring. *J. Atmos. Sci.*, **42**, 1711-1732.

Bolton, D., 1980: The computation of equivalent potential temperature. *Mon. Wea. Rev.*, **108**, 1046-1053.

Bunkers, M. J., B. A. Klimowski, J. Q. Zeitler, R. L. Thompson, M. L. Weisman, 2000: Predicting supercell motion using a new hodograph technique. *Wea. Forecasting*, **15**, 61-79.

Byers, H. R., and R. R. Braham Jr., 1949: *The thunderstorm.* U.S. Government Printing Office, 287pp.

Cressman, G. P., 1959: An operational objective analysis system. *Mon. Wea. Rev.*, **87**, 367-374.

Doswell, C. A., H. E. Brooks, and R. A. Maddox, 1996: Flash flood forecasting: An ingredients-based methodology. *Wea. Forecasting*, **11**, 560-581.

Doviak, R., and D. Zrnić, 1992: *Doppler radar and weather observations. Second edition.* Academic Press, 562pp.

Emanuel, K. A., 1994: *Atmospheric Convection.* Oxford University Press, 580pp.

Gascón, E., S. Laviola, A. Merino, and M. M. Miglietta, 2016: Analysis of a localized flash-flood event over the central Mediterranean, *Atmos. Res.*, **182**, 256-268.

Hamada, A., and Y. N. Takayabu, 2018: Large-scale environmental conditions related to midsummer extreme rainfall events around Japan in the TRMM region. *J. Climate*, **31**, 6933-6945.

Hamada, A., Y. N. Takayabu, C. Liu, and E. J. Zipser, 2015: Weak linkage between the heaviest rainfall and tallest storms. *Nat. Commun.*, **6**, 6213, doi:10.1038/ncomms7213.

Hirockawa, Y., T. Kato, H. Tsuguti, and N. Seino, 2020: Identification and classification of heavy rainfall areas and their characteristic features in Japan. *J. Meteor. Soc. Japan*, **98**, 835-857.

Houze Jr., R. A., 2012: Orographic effects on precipitating clouds, *Rev. Geophys.*, **50**, RG1001, doi:10.1029/2011RG000365.

Houze Jr., R. A., D. C. Wilton, and B. F. Smull, 2007: Monsoon convection in the Himalayan region as seen by the TRMM Precipitation Radar. *Quart. J. Roy. Meteor. Soc.*, **133**, 1389-1411.

Kato, T., 1998: Numerical simulation of the band-shaped torrential rain observed over southern Kyushu, Japan on 1 August 1993. *J. Meteor. Soc. Japan*, **76**, 97-128.

Kato, T., 2005: Statistical study of band-shaped rainfall systems, the Koshikijima and Nagasaki Lines, observed around Kyushu Island, Japan. *J. Meteor. Soc. Japan*, **83**, 943-957.

Kato, T., 2020: Quasi-stationary band-shaped precipitation systems, named as “senjo-kousuitai”, causing localized heavy rainfall in Japan. *J. Meteor. Soc. Japan*, **98**, 485- 509.

Kato, T., and K. Aranami, 2005: Formation factors of 2004 Niigata-Fukushima and Fukui heavy rainfalls and problems in the predictions using a cloud-resolving model. *SOLA*, **1**, 1-4.

Kawano, T., and R. Kawamura, 2020: Genesis and maintenance processes of a quasi-stationary convective band that produced record-breaking precipitation in northern Kyushu, Japan on 5 July 2017. *J. Meteor. Soc. Japan*, **98**, 673 – 690.

LeMone, M. A., E. J. Zipser, and S. B. Trier, 1998: The role of environmental shear and thermodynamic conditions in determining the structure and evolution of mesoscale convective systems during TOGA COARE. *J. Atmos. Sci.*, **55**, 3493–3518.

Morotomi, K., T. Shinoda, Y. Shusse, T. Kouketsu, T. Ohigashi, K. Tsuboki, H. Uyeda, and I. Tamagawa, 2012: Maintenance mechanisms of a precipitation band formed along the Ibuki-Suzuka mountains on September 2–3, 2008. *J. Meteor. Soc. Japan*, **90**, 737–753.

Ogura, Y., 1990: Analyses and mechanisms of intense precipitation. *Tenki*, **38**, 276-288 (in Japanese).

Oue, M., H. Uyeda, and Y. Shusse, 2010: Two types of precipitation particle distribution in convective cells accompanying a Baiu frontal rainband around Okinawa Island, Japan. *J. Geophys. Res.*, **115**, D02201, doi:10.1029/2009JD011957.

Oue, M., H. Uyeda, and D.-I. Lee, 2011: Raindrop size distribution parameters estimated from polarimetric radar variables in convective cells around Okinawa Island during the Baiu period. *Asia-Pac. J. Atmos. Sci.*, **47**, 33-44.

Oue, M., K. Inagaki, T. Shinoda, T. Ohigashi, T. Koketsu, M. Kato, K. Tsuboki, and H. Uyeda, 2014: Polarimetric Doppler radar analysis of organization of a stationary rainband with changing orientations in July 2010. *J. Meteor. Soc. Japan*, **92**, 457-481.

Pontrelli, M. D., G. Bryan, and J. M. Fritsch, 1999: The Madison County, Virginia, flash flood of 27 June 1995. *Wea. Forecasting*, **14**, 384–404.

Seko, H., and H. Nakamura, 2003: Numerical study of the shapes and maintenance mechanisms of meso-β scale line-shaped precipitation system in the middle-latitudes. *CAS/JSC WGNE Res. Activ. Atmos. Oceanic Modell.*, **33**, 5.30–5.31.

Shumacher, R. S., and R. H. Johnson, 2005: Organization and environmental properties of extreme-rain-producing mesoscale convective systems. *Mon. Wea. Rev.*, **133**, 961-976.

Smith, R. B., 1989: Hydrostatic airflow over mountains. *Adv. Geophys.*, **31**, 1-41.

Smith, R. B., 2019: 100 years of progress on mountain meteorology research. *Meteor. Monogr.*, **59**, 20.1 – 20.73.

Smolarkiewicz, P. K., and R. Rotunno, 1989: Low Froude number flow past three-dimensional obstacles. part I: B9aroclinically generated lee vortices., *J. Atmos. Sci.*, **46**, 1154-1164.

Sohn, B.-J., G.-H. Ryu, H.-J. Song, and M.-L. Ou, 2013: Characteristic features of warm-type rain producing heavy rainfall over the Korean Peninsula inferred from TRMM measurements. *Mon. Wea. Rev.* **141**, 3873–3888.

Umemoto, Y., M. Teshiba, Y. Shibagaki, H. Hashiguchi, M. D. Yamanaka, S. Fukao, and X-BAIU-99 and X-AIU-02 observational groups, 2004: Combined wind profiler-weather radar observations of orographic rainband around Kyushu, Japan in the Baiu season. *Ann. Geophys.*, **22**, 3971-3982.

Umemoto, Y., H. Hashiguchi, S. Fukao, and M. Teshiba, 2005: Wind variations around orographic rainband observed by wind profiler network in Japan. *Proc. of 11th Conference on Mesoscale Processes*, JP7J.7. [Available at https://ams.confex.com/ams/32Rad11Meso/webprogram/Paper97171.html.]

Unuma, T., and F. Murata, 2012: Statical analysis of quasi-stationary line-shaped rainfall systems over Shikoku Island, Japan. *Tenki*, **59**, 119-125 (in Japanese).

Unuma, T., and T. Takemi, 2016a: Characteristics and environmental conditions of quasi‐stationary convective clusters during the warm season in Japan. *Quart. J. Roy. Meteor. Soc.*, **142**, 1232–1249.

Unuma, T., and T. Takemi, 2016b: A role of environmental shear on the organization mode of quasi-stationary convective clusters during the warm season in Japan. *SOLA*, **12**, 111–115.

Watanabe, H., and Y. Ogura, 1987: Effects of orographically forced upstream lifting on mesoscale heavy precipitation: A case study. *J. Atmos. Sci.*, **44**, 661-675.

Yoshizaki, M., T. Kato, Y. Tanaka, H. Takayama, M. Tanaka, and Members of X-BAIU 98 observation, 2000: Analytical and numerical study of the 26 June 1998 orographic rainband observed in western Kyushu, Japan. *J. Meteor. Soc. Japan*, **78**, 835–856.

Yu, C.-K., and Y.-H. Hsieh, 2009: Formation of the convective lines off the mountainous coast of southeastern Taiwan: A case study of 3 January 2004. *Mon. Wea. Rev.*, **137**, 3072–3091.

Yu, C.-K., W.-F. Liu, L.-W. Cheng, and C.-Y. Lin, 2022: Mechanisms of valley precipitation enhancement over Da-Tun Mountain. *Mon. Wea. Rev.*, **150**, 1851-1871.

Yuter, S. E, and R. A. Houze Jr.,1995: Three-dimensional kinematic and microphysical evolution of Florida cumulonimbus. Part II: Frequency distributions of vertical velocity, reflectivity, and differential reflectivity. *Mon. Wea. Rev.*, **123**, 1941-1963.

Zhang, C. Z., H. Uyeda, H. Yamada, B. Geng, and Y. Ni, 2006: Characteristics of mesoscale convective systems over east part of continental China during the Meiyu from 2001 to 2003. *J. Meteor. Soc. Japan*, **84**, 763–782.

List of Figures

Fig. 1 (a) Location of Shikoku and orography (shaded). The red-dashed rectangle indicates the area displayed in (b), while the blue-dashed rectangle denotes display areas of (c) and (d). (b) Distributions of orography (shaded) in the area surrounded by the red rectangle in (a). Areas enclosed by red-solid lines are the large-scale views of orography defined in this study (see text for details). A blue-dashed circle indicates the location of the Muroto Peninsula. Small-scale features in the Muroto Peninsula which will be described in this study are shown in a lower-right panel. Blue- and red-dotted lines show the locations of small-scale concave valleys (CV1 and CV2) and a ridge (SR), respectively. (c) Accumulated rainfall observed by XRAIN from 12–20 JST on July 3, 2018 (colored contours) and the locations of observations. A red square, a blue triangle, and a green circle represent the locations of JMA AMeDAS at Kaiyo, JMA AMeDAS and JMA operational weather radar at Murotomisaki, and JMA wind profiler at Kochi, respectively. A yellow triangle represents the location of one of the XRAIN C-band polarimetric radars. (d) Same as (c), but for 16-21 JST on August 15, 2018.

Fig. 2 Snapshots of horizontal reflectivity (Z_h) observed by JMA Murotomisaki radar. (a) A horizontal cross section at 2 km in height analyzed by Plan Position Indicator (PPI) scans observed from 1733 to 1738 JST on July 3, 2018. No-data areas are indicated by gray shading. (b) A vertical cross section along a dashed line shown in (a). (c) Same as (a), but for 1743–1748 JST on August 15, 2018. (d) Same as (b), but for along a dashed line shown in (c).

Fig. 3 Horizontal distributions of hourly rainfall derived from XRAIN between 11 and 21 JST on July 3, 2018. The maximum values of hourly rainfall for each period are displayed in the lower-right corner of each figure.

Fig. 4 Same as Fig. 3, but for between 15 and 22 JST on August 15, 2018.

Fig. 5 JMA surface weather charts analyzed at (a) 09 JST, on July 3, 2018, and (b) 15 JST on August 15, 2018. (c) (d) Horizontal distribution of equivalent potential temperature at the 950 hPa level (shaded), horizontal wind at the 950 hPa level (vectors), and geopotential height at the 500 hPa level (black contours) derived from the initial value of JMA-MSM on the same time as (a) and (b), respectively. The location of Shikoku is indicated by a red rectangle.

Fig. 6 (a) Skew-T log-p diagram and (b) Vertical profiles of relative humidity collected from the initial value of JMA-MSM. Red and blue solid lines in (a) indicate vertical profiles of temperature and dew-point temperature, respectively. Solid lines (dashed lines) represent the profile for 12 JST on July 3, 2018 (15 JST on August 15, 2018). Each value is a horizontal average within a red dashed rectangle (3 x 3 grids) shown in the lower-left map of (a).

Fig. 7 Time series of (a) wind speed, (b) wind direction, (c) water vapor mixing ratio, (d) water vapor flux (WVF), and (e) potential temperature observed by JMA surface weather station at Murotomisaki (solid line) and Kaiyo (dashed line, only shown in potential temperature) from 09 to 24 JST on July 3, 2018. (f)–(j) Same as (a)–(e), but for from 13 to 24 JST on August 15, 2018. The gray-shaded periods represent times beyond the scope of this study. The locations of Murotomisaki and Kaiyo are shown in Fig. 1.

Fig. 8 Hodographs of horizontal wind observed by JMA wind profiler at Kochi (circles) and JMA surface weather station at Murotomisaki (stars) averaged during (a) Case 1A (12 to 15 JST on July 3, 2018), (b) Case 1B (17 to 20 JST on July 3, 2018), and (c) Case 2 (16 to 21 JST on August 15, 2018). The colors of plots indicate the observation height. Red dashed lines indicate the orientation angles of the MLs obtained by averaging the orientations of hourly rainfall area 20 mm or grater during each period.

Fig. 9 Time-latitude section of maximum rainfall intensity between 134.1°E and 134.4°E obtained from XRAIN during Case 1 (from 12 JST to 20 JST on July 3, 2018). The orography in the analyzed area is shown on the left panel. The orientation of arrows indicates the representative latitudinal moving speed of convective cells. A red-dashed line in the left panel indicates the latitude of a time-longitude cross section shown in Fig. 11a.

Fig. 10 Same as Fig. 9, but for maximum rainfall intensity between 134.15 °E and 134.45 °E during Case 2 (from 16 JST to 21 JST on August 15, 2018). A red-dashed line in the left panel indicates the latitude of a time-longitude cross section shown in Fig. 11a.

Fig. 11 Time-longitude cross section of XRAIN rainfall intensity (a) at 33.50°N during Case 1 (from 12 to 20 JST on July 3, 2018) and (b) at 33.45°N during Case 2 (from 16 to 21 JST on August 15, 2018). A black dashed circle indicates a weak band formed west of the ML.

Fig. 12 Horizontal distribution of mean rainfall intensity (colored contour) derived from XRAIN and orography (shade) for (a) Case 1A (from 12 to 15 JST on July 3, 2018). A red-dashed rectangle indicates the displaying area of (b), (d), and (f). A red-dotted rectangle shows the analysis area of Fig. 13. (b) Enlarged display of (a) focusing on the southern part of the ML. Purple-dotted line displays the location of the SR small-scale ridge. Light- and dark-blue-dotted lines indicate locations of small-scale concave valleys named CV1 and CV2, respectively. (c) (d) Same to (a) and (b), respectively, but for Case 1B (from 17 to 20 JST on July 3, 2018). (e) (f) Same to (a) and (b), respectively, but for Case 2 (from 16 to 21 JST on August 15, 2018). Black-dashed rectangles and alphabets in (c) and (e) represent CFAD analyses areas and subcaptions in Fig. 14.

Fig. 13 Appearance frequency of the zonal maximum echo-top height obtained from JMA Murotomisaki CAPPI data (shaded) and the zonal maximum value of mean XRAIN rainfall intensity (solid curve). (a) (b) Maximum 15 dBZ and 35 dBZ echo-top height between 134.10°E and 134.25°E during Case 1A (from 12 to 15 JST on July 3, 2018), respectively. Solid, dashed, and dotted horizontal lines show the 0 °C, -10 °C, and -20 °C height derived from Fig. 6, respectively. (c) (d) Same to (a) and (b), respectively, but for the maximum values between 134.15°E and 134.40°E during Case 1B (from 17 to 20 JST on July 3, 2018). (e) (f) Same to (a) and (b), respectively, but for the maximum values between 134.15°E and 134.45°E during Case 2 (from 16 to 21 JST on August 15, 2018).

Fig. 14 Normalized Contoured Frequency Altitude Diagrams (CFADs) of horizontal reflectivity (Z_h) obtained from JMA Murotomisaki CAPPI data sampled at (a) the heaviest rainfall area, (b) the southernmost part of the HR area during Case 1B (from 17 to 20 JST on July 3, 2018). The analysis areas of each figure are displayed in Fig. 12. A bold solid curve indicates the vertical profile of the median of Z_h. The thin solid, dashed, and dotted horizontal lines show the 0 °C, -10 °C, and -20 °C levels derived from Fig. 6, respectively.

The data below 1.5 km in height is masked by gray shade due to the lack of observation. The right panel of each figure shows the logarithmic number of samples at each height. (c), (d) same to as (a) and (b) respectively, but during Case 2 (from 16 to 21 JST on August 15, 2018).

Fig. 1

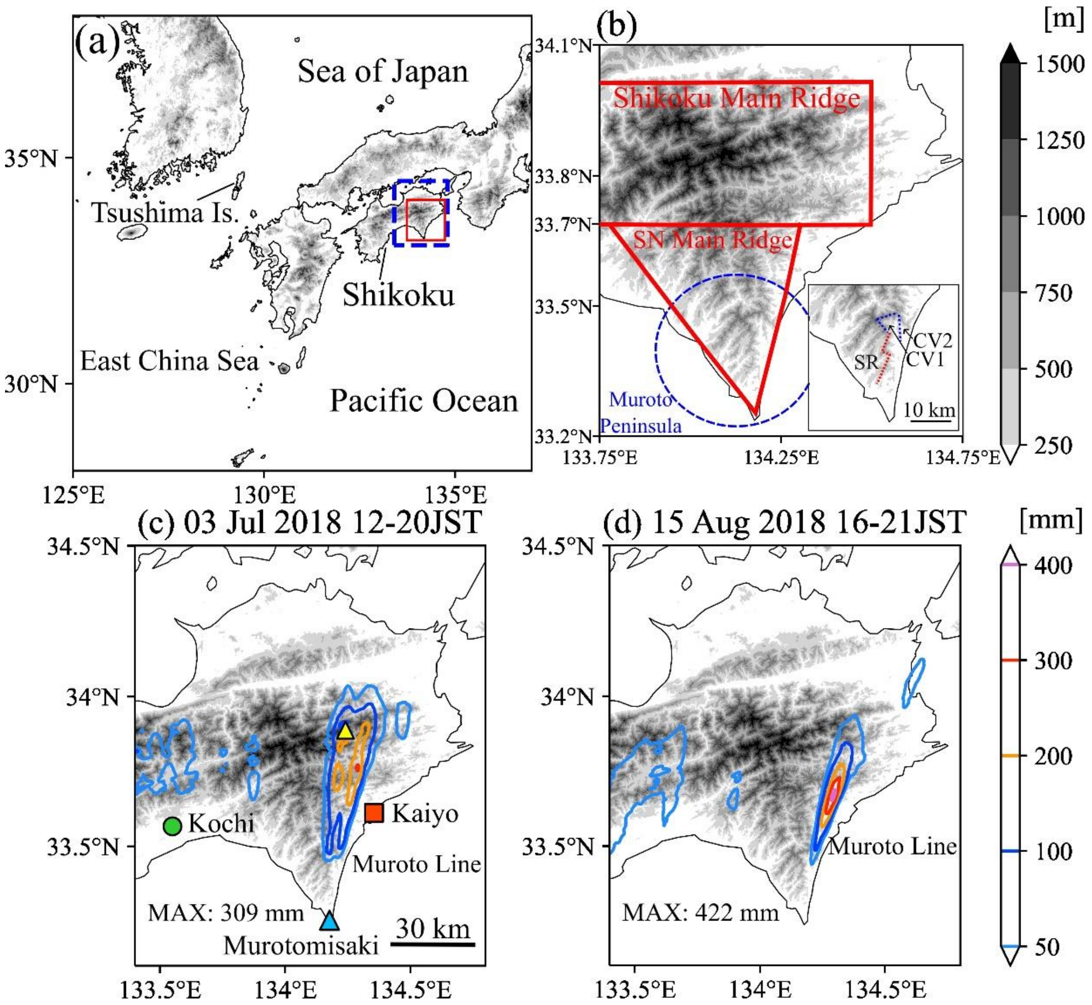

Fig. 1 (a) Location of Shikoku and orography (shaded). The red-dashed rectangle indicates the area displayed in (b), while the blue-dashed rectangle denotes display areas of (c) and (d). (b) Distributions of orography (shaded) in the area surrounded by the red rectangle in (a). Areas enclosed by red-solid lines are the large-scale views of orography defined in this study (see text for details). A blue-dashed circle indicates the location of the Muroto Peninsula. Small-scale features in the Muroto Peninsula which will be described in this study are shown in a lower-right panel. Blue- and red-dotted lines show the locations of small-scale concave valleys (CV1 and CV2) and a ridge (SR), respectively.

(c) Accumulated rainfall observed by XRAIN from 12–20 JST on July 3, 2018 (colored contours) and the locations of observations. A red square, a blue triangle, and a green circle represent the locations of JMA AMeDAS at Kaiyo, JMA AMeDAS and JMA operational weather radar at Murotomisaki, and JMA wind profiler at Kochi, respectively. A yellow triangle represents the location of one of the XRAIN C-band polarimetric radars.

(d) Same as (c), but for 16-21 JST on August 15, 2018.

Fig. 2

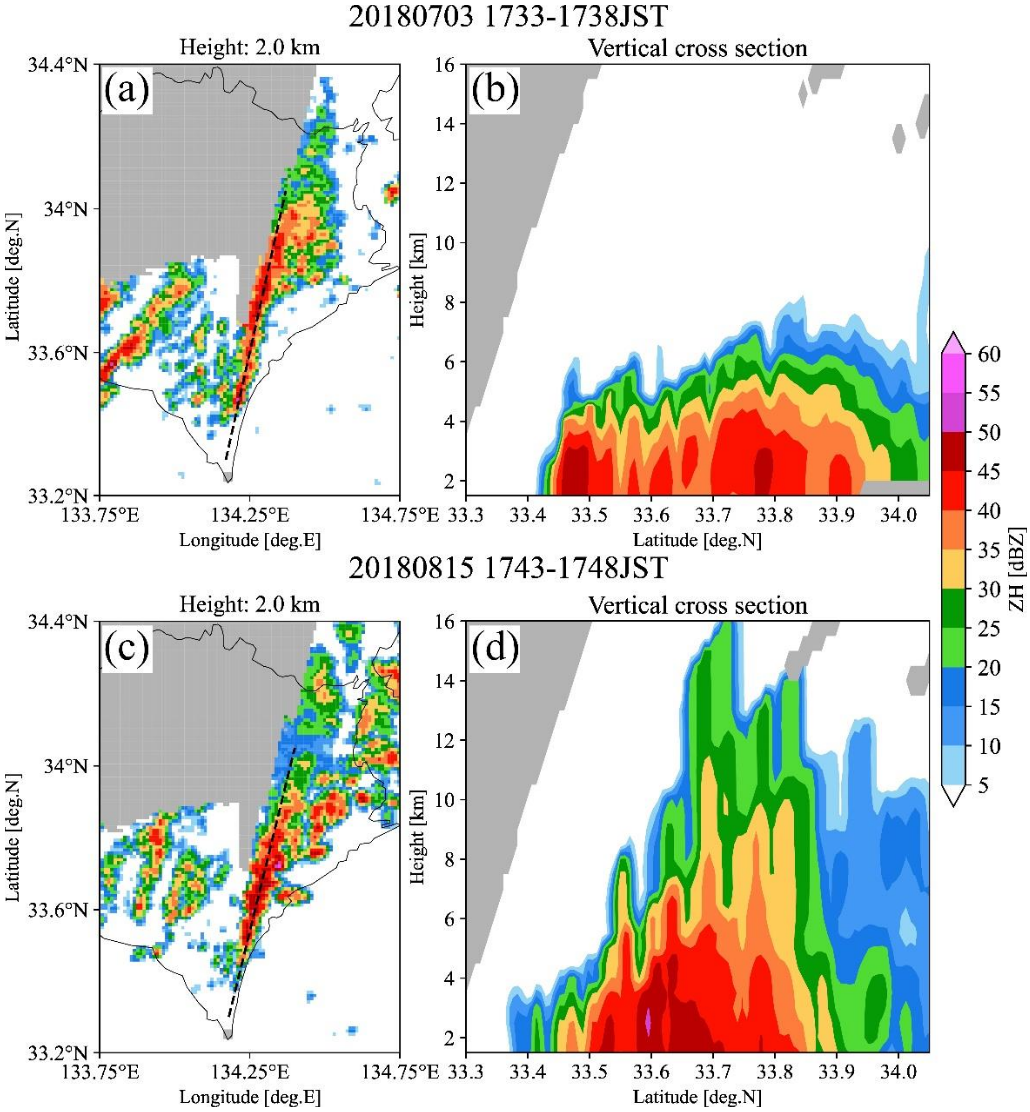

Fig. 2 Snapshots of horizontal reflectivity (Z_h) observed by JMA Murotomisaki radar. (a) A horizontal cross section at 2 km in height analyzed by Plan Position Indicator (PPI) scans observed from 1733 to 1738 JST on July 3, 2018. No-data areas are indicated by gray shading. (b) A vertical cross section along a dashed line shown in (a). (c) Same as (a), but for 1743–1748 JST on August 15, 2018. (d) Same as (b), but for along a dashed line shown in (c).

Fig. 3

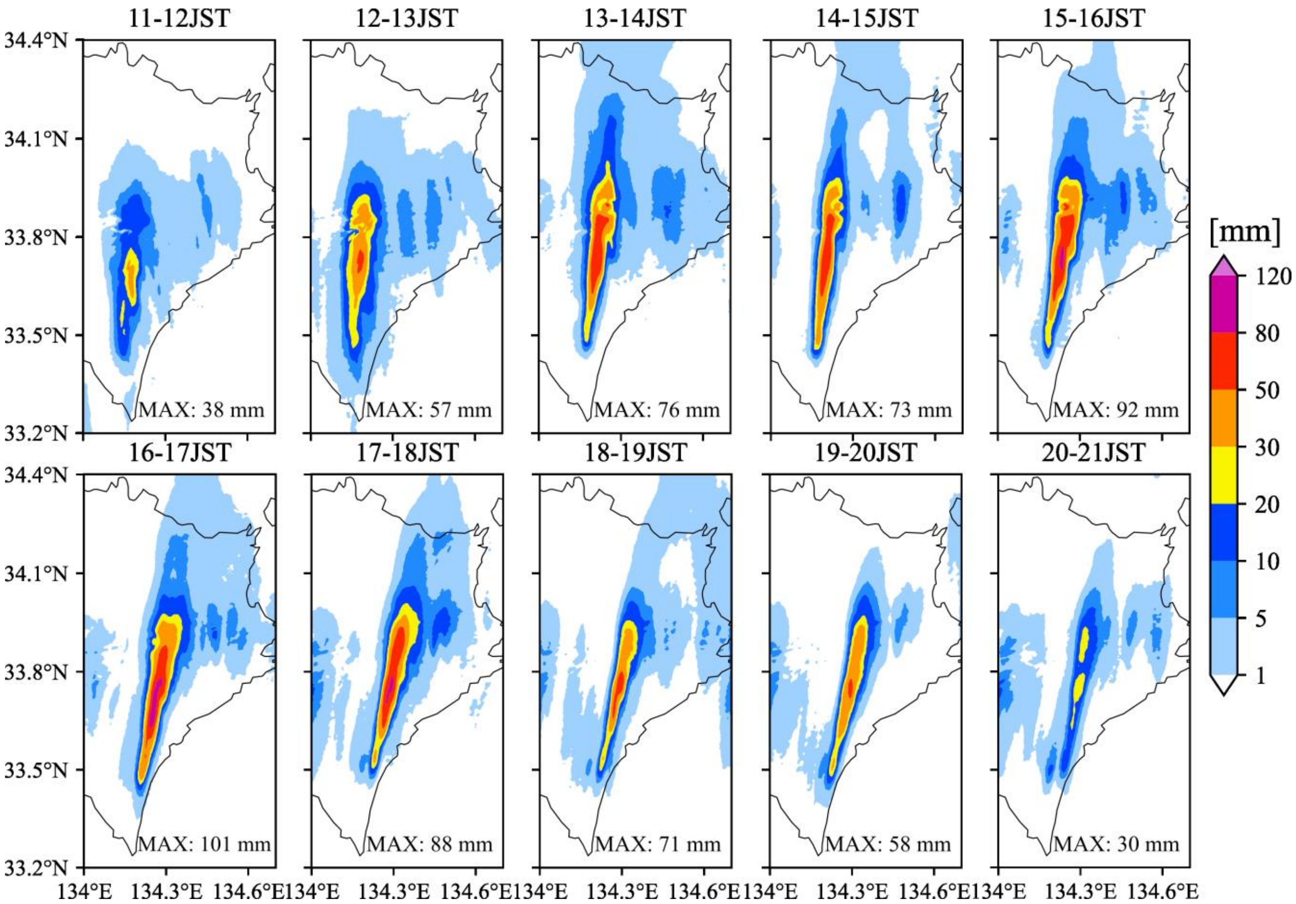

Fig. 3 Horizontal distributions of hourly rainfall derived from XRAIN between 11 and 21 JST on July 3, 2018. The maximum values of hourly rainfall for each period are displayed in the lower-right corner of each figure.

Fig. 4

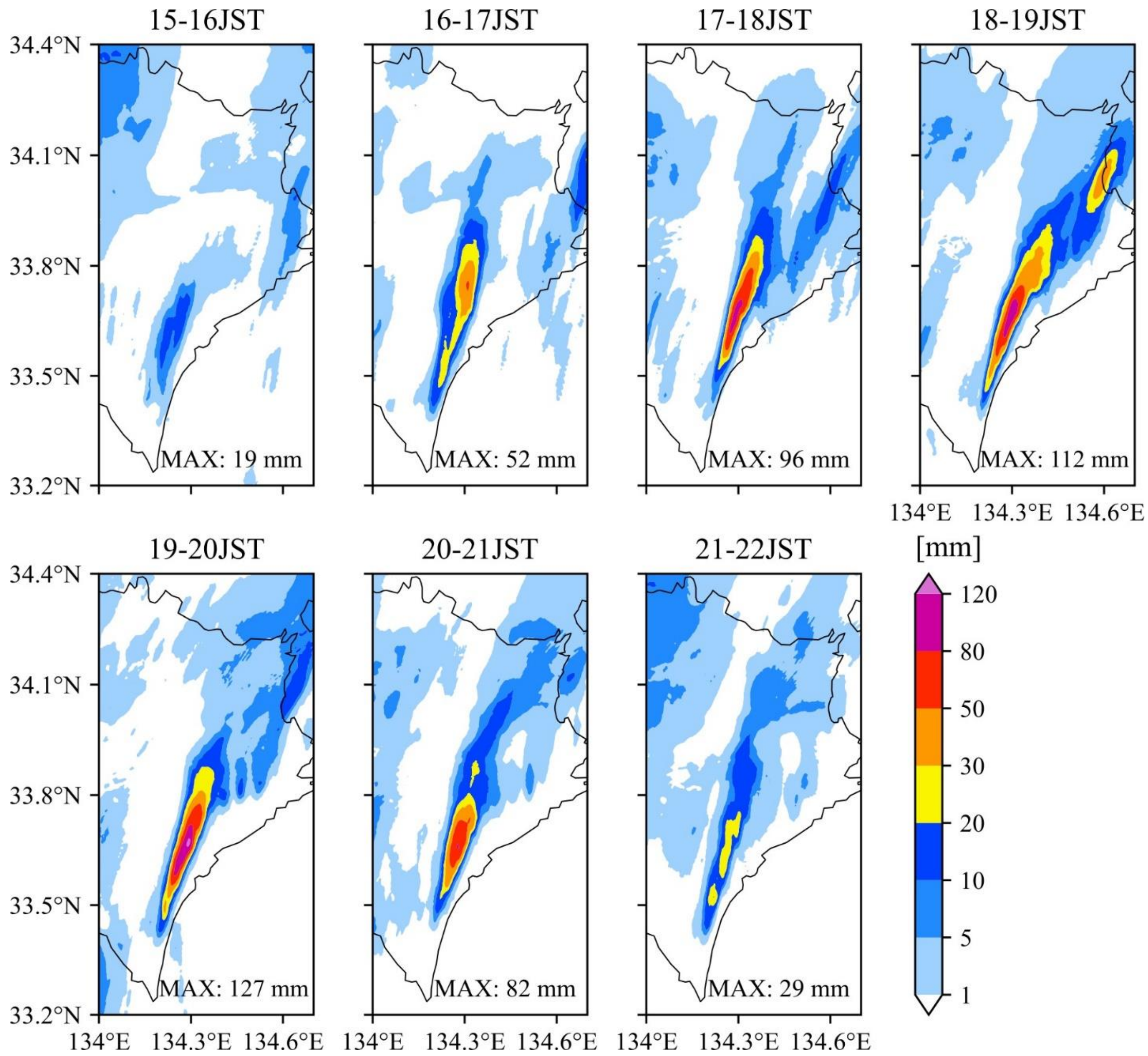

Fig. 4 Same as Fig. 3, but for between 15 and 22 JST on August 15, 2018.

Fig. 5

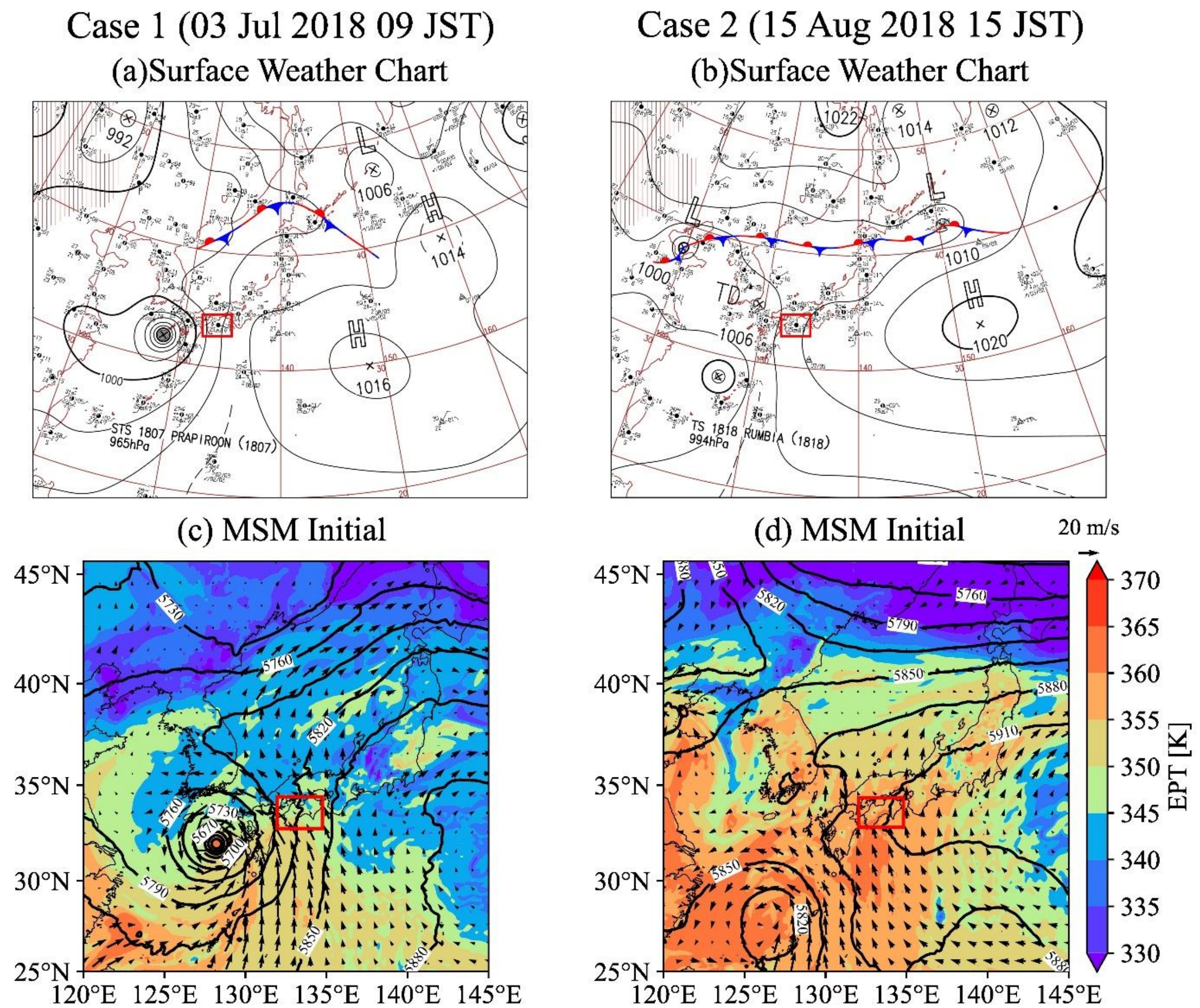

Fig. 5 JMA surface weather charts analyzed at (a) 09 JST, on July 3, 2018, and (b) 15 JST on August 15, 2018. (c) (d) Horizontal distribution of equivalent potential temperature at the 950 hPa level (shaded), horizontal wind at the 950 hPa level (vectors), and geopotential height at the 500 hPa level (black contours) derived from the initial value of JMA-MSM on the same time as (a) and (b), respectively. The location of Shikoku is indicated by a red rectangle.

Fig. 6

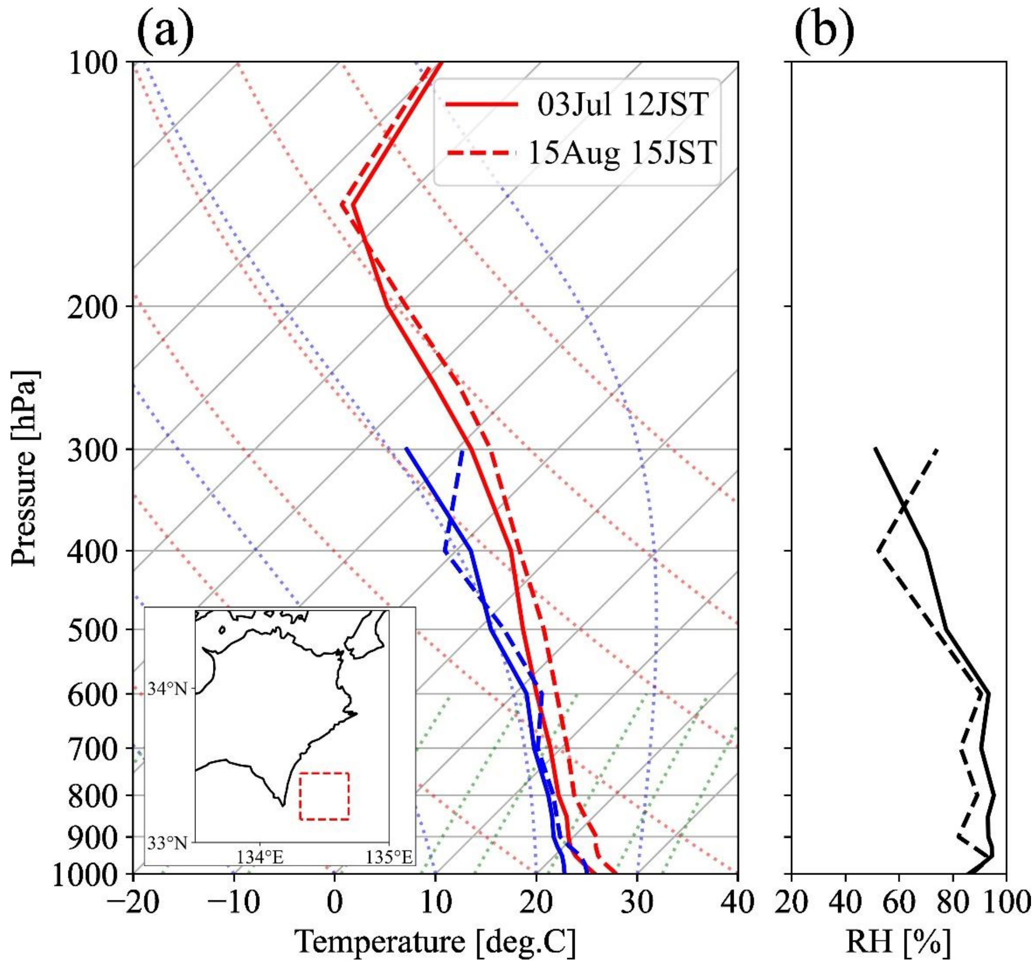

Fig. 6 (a) Skew-T log-p diagram and (b) Vertical profiles of relative humidity collected from the initial value of JMA-MSM. Red and blue solid lines in (a) indicate vertical profiles of temperature and dew-point temperature, respectively. Solid lines (dashed lines) represent the profile for 12 JST on July 3, 2018 (15 JST on August 15, 2018). Each value is a horizontal average within a red dashed rectangle (3 x 3 grids) shown in the lower-left map of (a).

Fig. 7

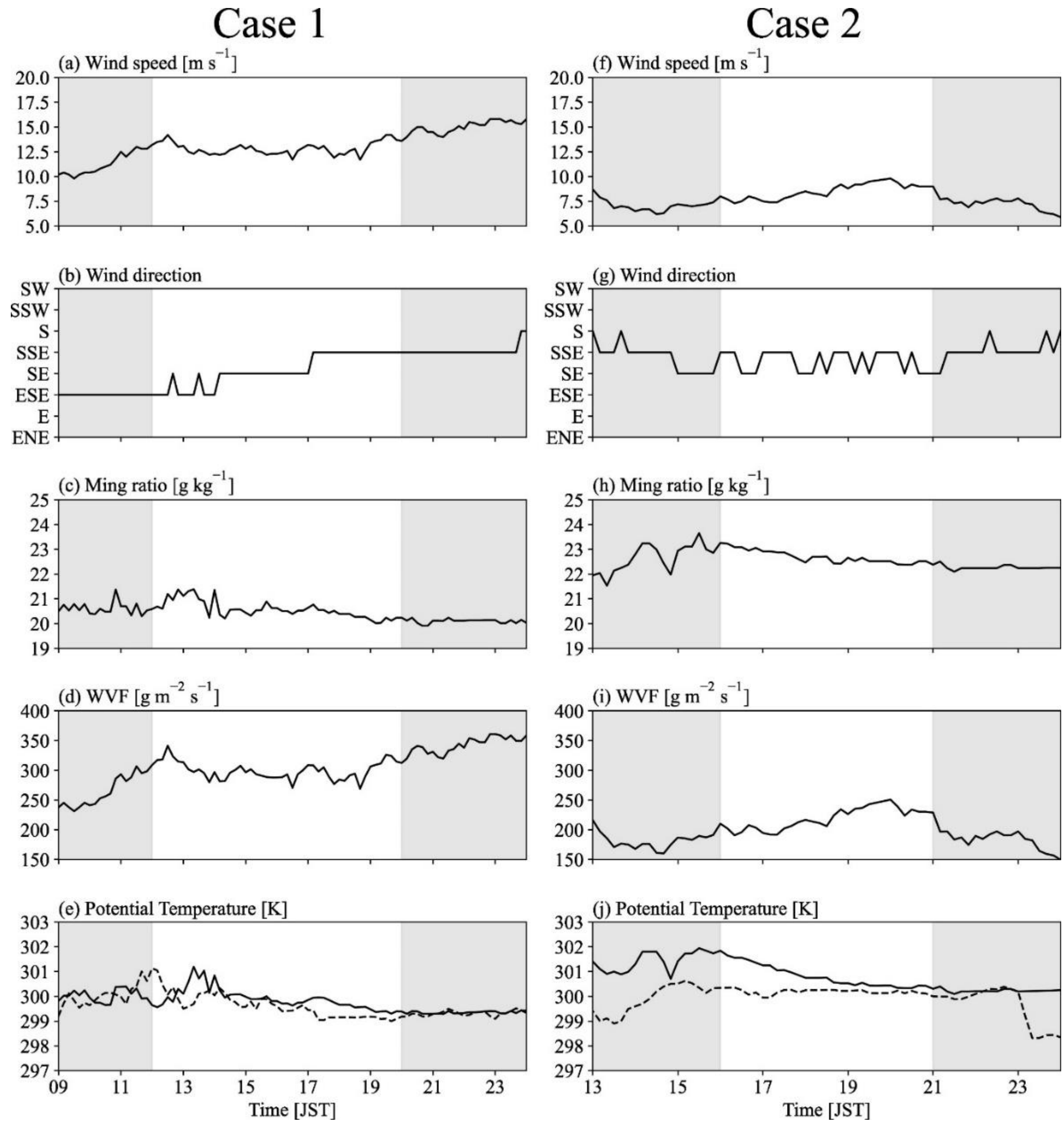

Fig. 7 Time series of (a) wind speed, (b) wind direction, (c) water vapor mixing ratio, (d) water vapor flux (WVF), and (e) potential temperature observed by JMA surface weather station at Murotomisaki (solid line) and Kaiyo (dashed line, only shown in potential temperature) from 09 to 24 JST on July 3, 2018. (f)–(j) Same as (a)–(e), but for from 13 to 24 JST on August 15, 2018. The gray-shaded periods represent times beyond the scope of this study. The locations of Murotomisaki and Kaiyo are shown in Fig. 1.

Fig. 8

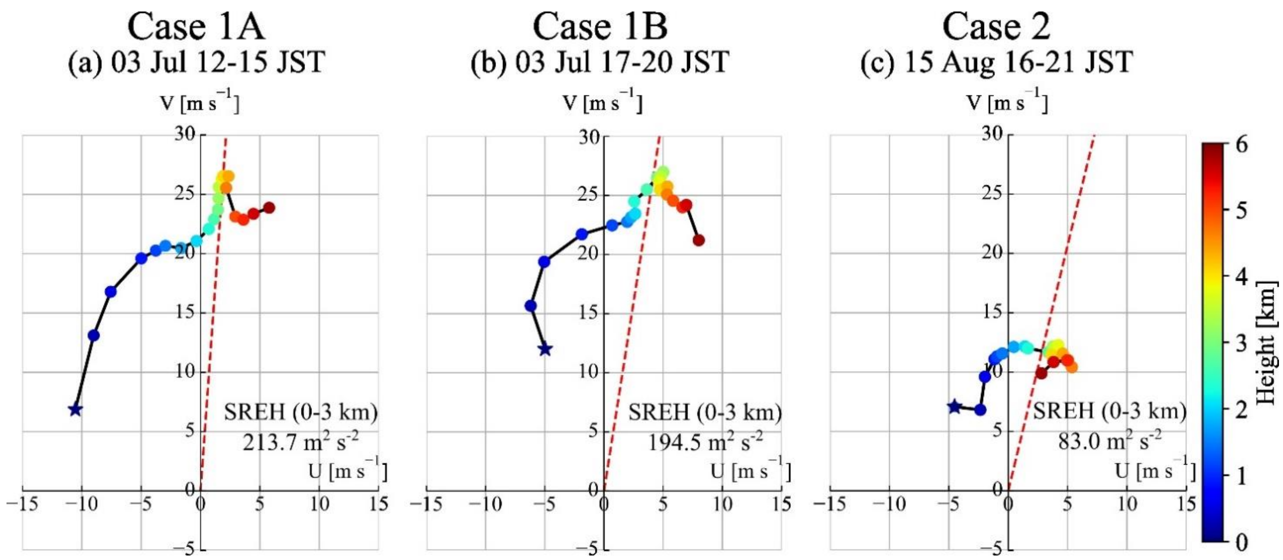

Fig. 8 Hodographs of horizontal wind observed by JMA wind profiler at Kochi (circles) and JMA surface weather station at Murotomisaki (stars) averaged during (a) Case 1A (12 to 15 JST on July 3, 2018), (b) Case 1B (17 to 20 JST on July 3, 2018), and (c) Case 2 (16 to 21 JST on August 15, 2018). The colors of plots indicate the observation height. Red dashed lines indicate the orientation angles of the MLs obtained by averaging the orientations of hourly rainfall area 20 mm or grater during each period.

Fig. 9

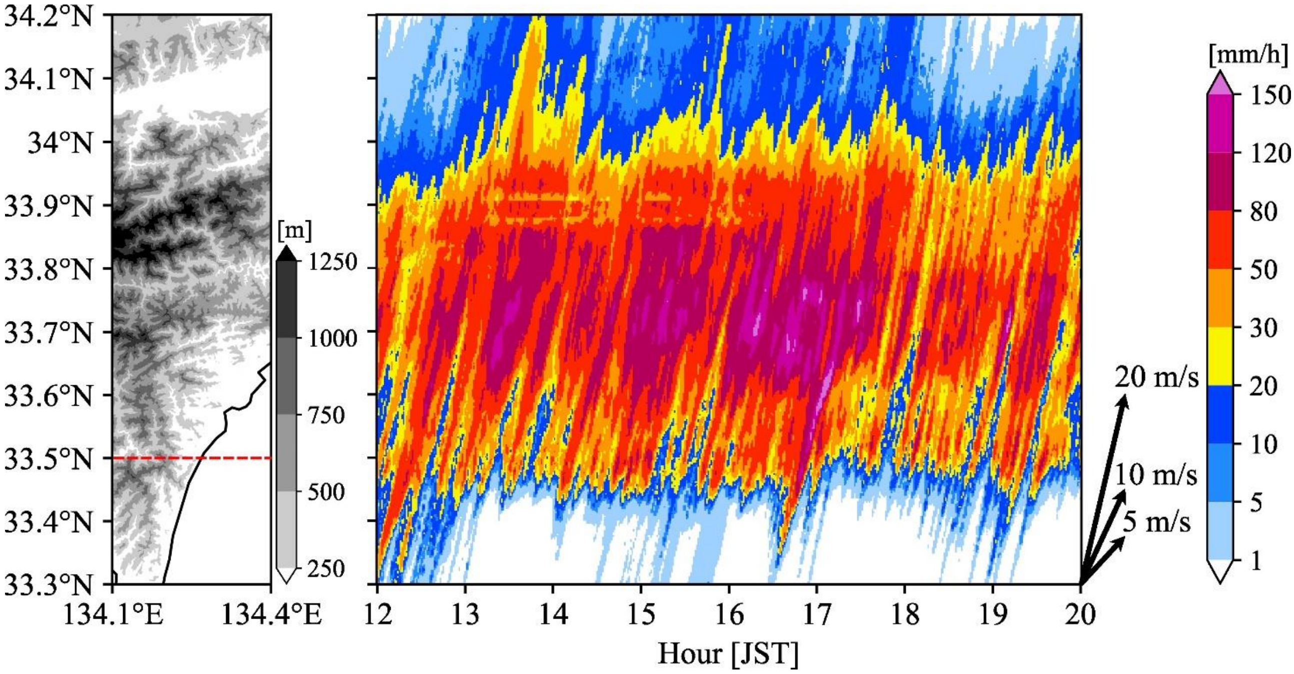

Fig. 9 Time-latitude section of maximum rainfall intensity between 134.1°E and 134.4°E obtained from XRAIN during Case 1 (from 12 JST to 20 JST on July 3, 2018). The orography in the analyzed area is shown on the left panel. The orientation of arrows indicates the representative latitudinal moving speed of convective cells. A red-dashed line in the left panel indicates the latitude of a time-longitude cross section shown in Fig. 11a.

Fig. 10

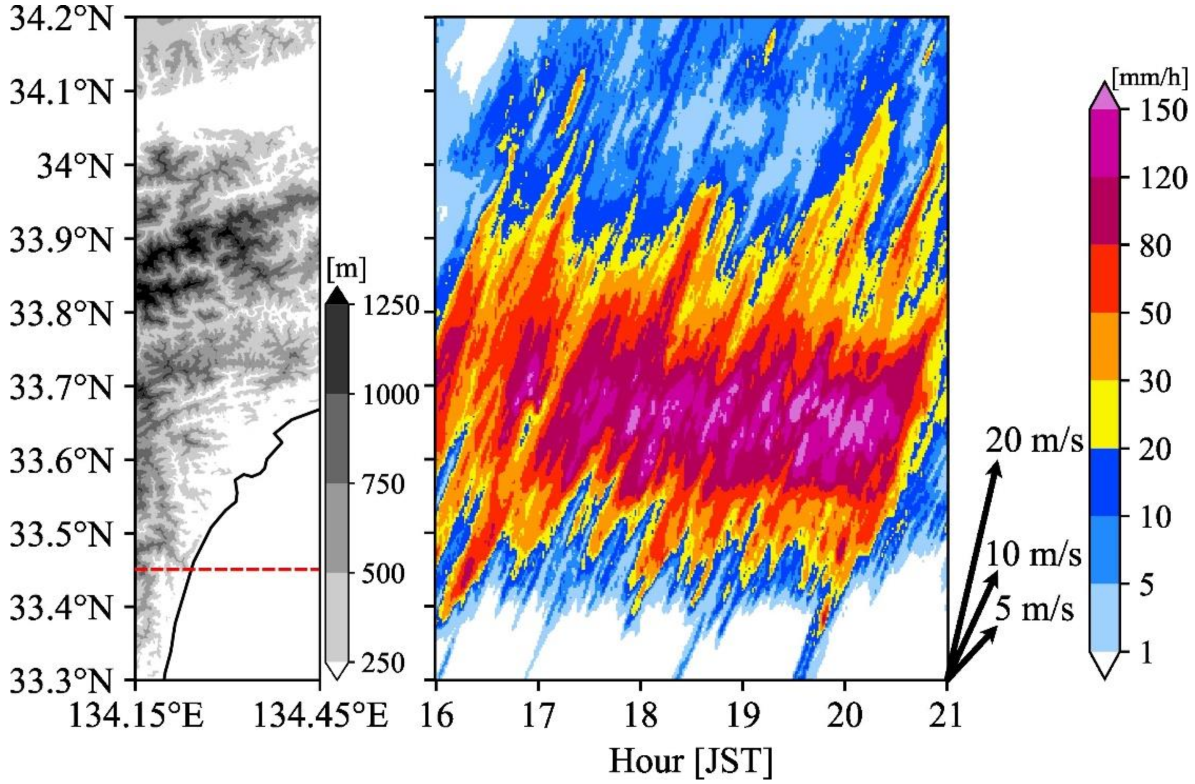

Fig. 10 Same as Fig. 9, but for maximum rainfall intensity between 134.15 °E and 134.45 °E during Case 2 (from 16 JST to 21 JST on August 15, 2018). A red-dashed line in the left panel indicates the latitude of a time-longitude cross section shown in Fig. 11a.

Fig. 11

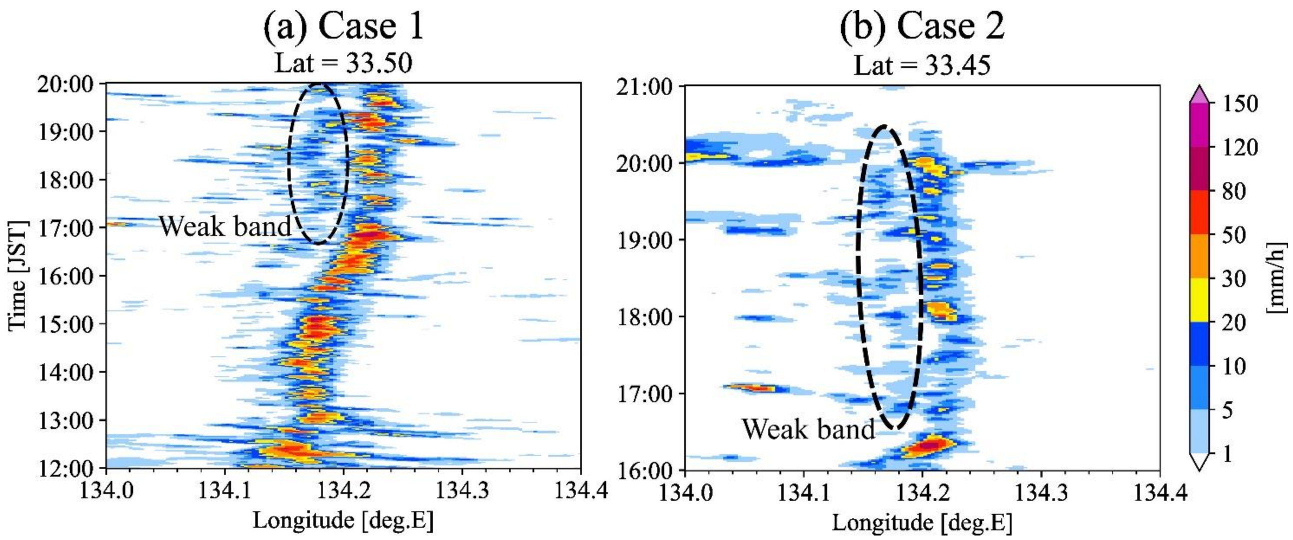

Fig. 11 Time-longitude cross section of XRAIN rainfall intensity (a) at 33.50°N during Case 1 (from 12 to 20 JST on July 3, 2018) and (b) at 33.45°N during Case 2 (from 16 to 21 JST on August 15, 2018). A black dashed circle indicates a weak band formed west of the ML.

Fig. 12

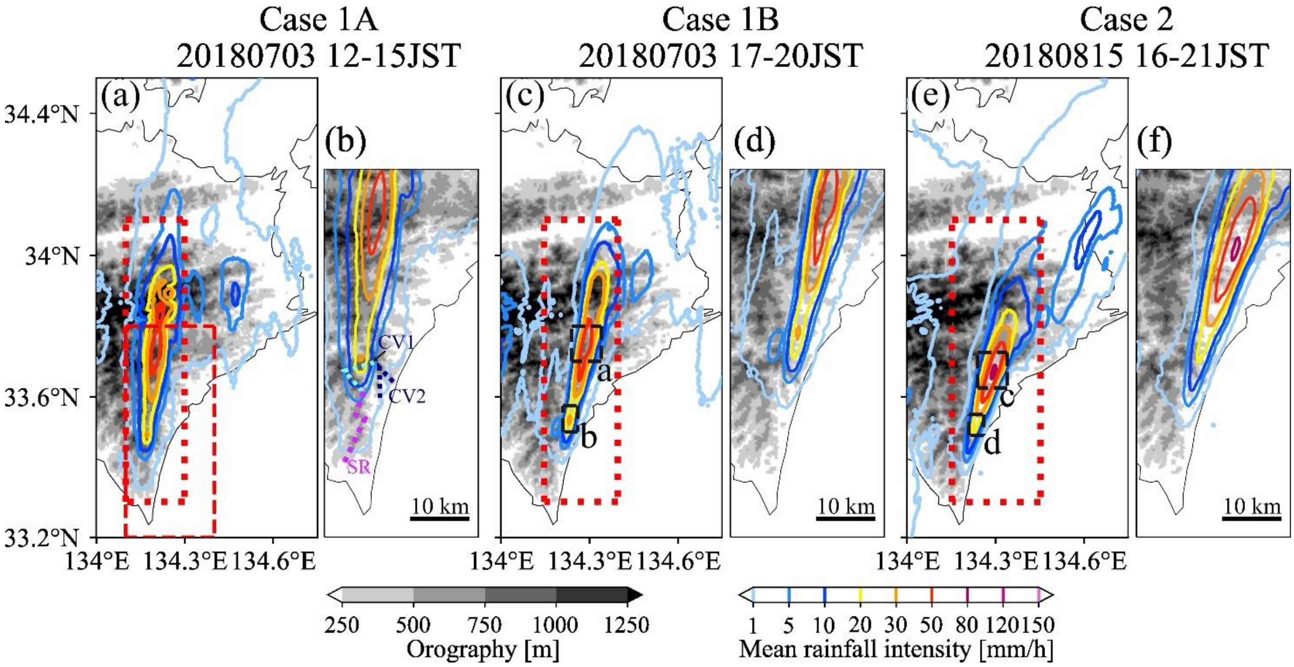

Fig. 12 Horizontal distribution of mean rainfall intensity (colored contour) derived from XRAIN and orography (shade) for (a) Case 1A (from 12 to 15 JST on July 3, 2018). A red-dashed rectangle indicates the displaying area of (b), (d), and (f). A red-dotted rectangle shows the analysis area of Fig. 13. (b) Enlarged display of (a) focusing on the southern part of the ML. Purple-dotted line displays the location of the SR small-scale ridge. Light- and dark-blue-dotted lines indicate locations of small-scale concave valleys named CV1 and CV2, respectively. (c) (d) Same to (a) and (b), respectively, but for Case 1B (from 17 to 20 JST on July 3, 2018). (e) (f) Same to (a) and (b), respectively, but for Case 2 (from 16 to 21 JST on August 15, 2018). Black-dashed rectangles and alphabets in (c) and (e) represent CFAD analyses areas and subcaptions in Fig. 14.

Fig. 13

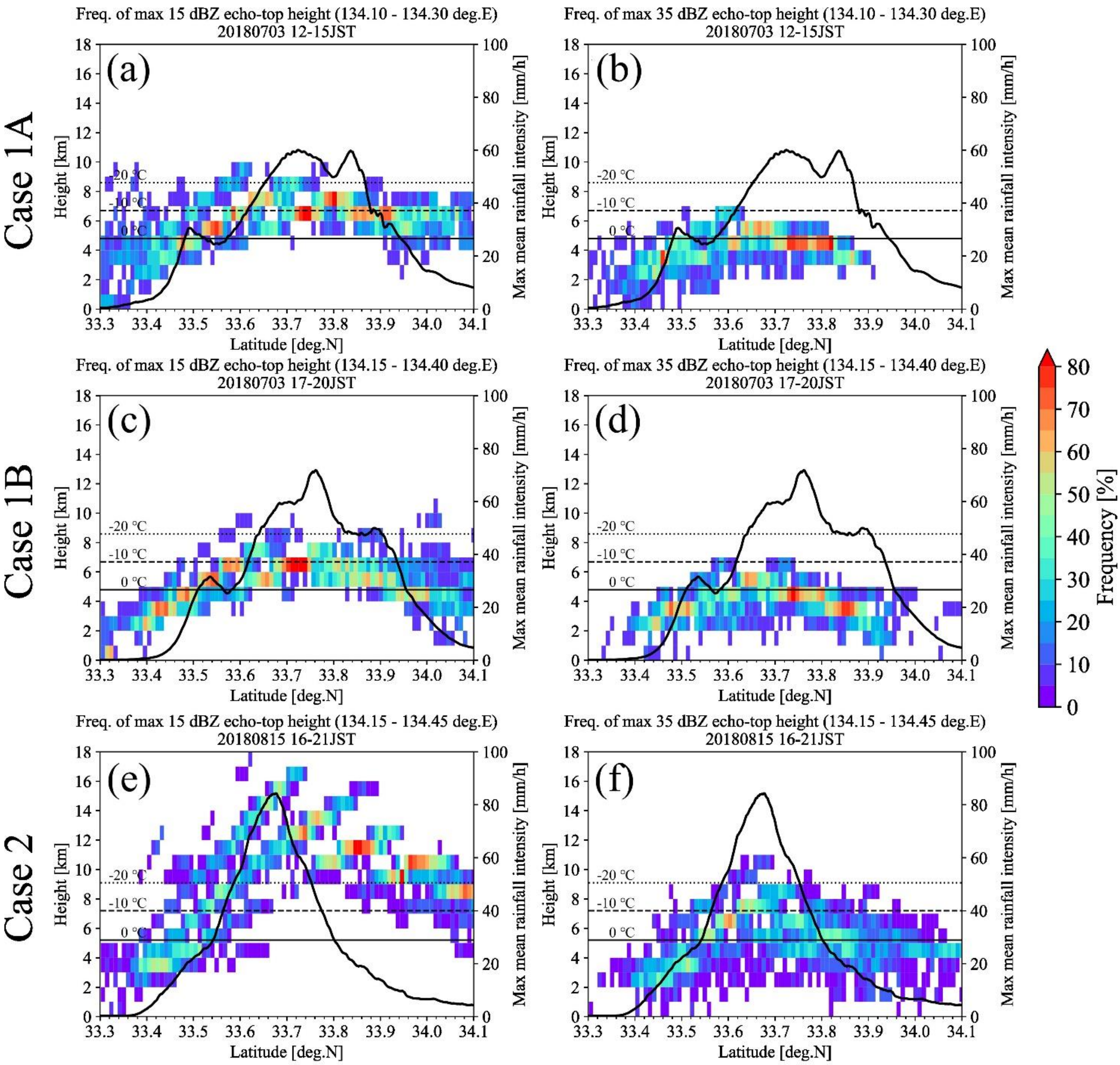

Fig. 13 Appearance frequency of the zonal maximum echo-top height obtained from JMA Murotomisaki CAPPI data (shaded) and the zonal maximum value of mean XRAIN rainfall intensity (solid curve). (a) (b) Maximum 15 dBZ and 35 dBZ echo-top height between 134.10°E and 134.25°E during Case 1A (from 12 to 15 JST on July 3, 2018), respectively. Solid, dashed, and dotted horizontal lines show the 0 °C, -10 °C, and -20 °C height derived from Fig. 6, respectively. (c) (d) Same to (a) and (b), respectively, but for the maximum

values between 134.15°E and 134.40°E during Case 1B (from 17 to 20 JST on July 3, 2018). (e) (f) Same to (a) and (b), respectively, but for the maximum values between 134.15°E and 134.45°E during Case 2 (from 16 to 21 JST on August 15, 2018).

Fig. 14

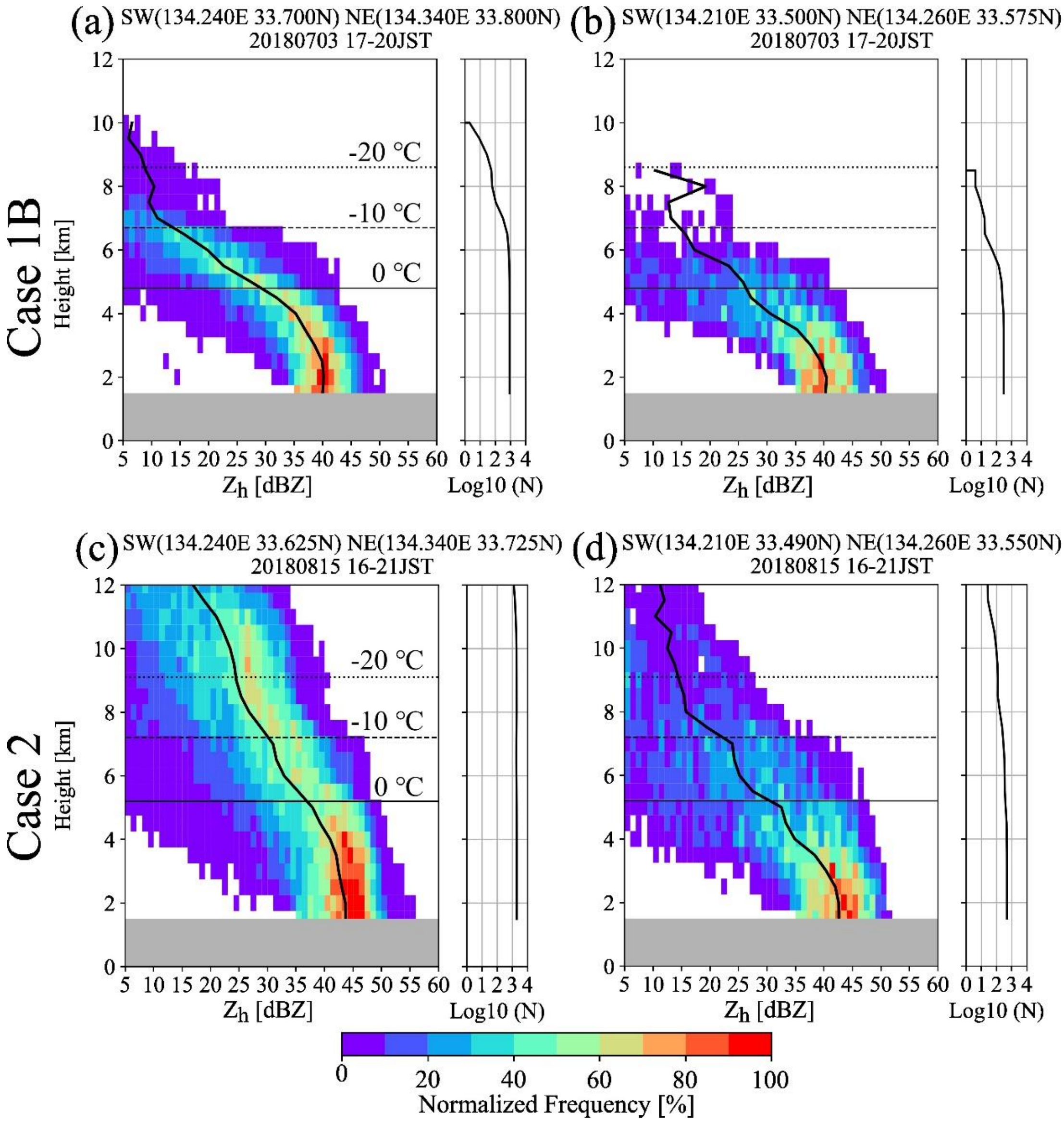

Fig. 14 Normalized Contoured Frequency Altitude Diagrams (CFADs) of horizontal reflectivity (Z_h) obtained from JMA Murotomisaki CAPPI data sampled at (a) the heaviest rainfall area, (b) the southernmost part of the HR area during Case 1B (from 17 to 20 JST on July 3, 2018). The analysis areas of each figure are displayed in Fig. 12. A bold solid curve indicates the vertical profile of the median of Z_h. The thin solid, dashed, and dotted horizontal lines show the 0 °C, -10 °C, and -20 °C levels derived from Fig. 6, respectively.

The data below 1.5 km in height is masked by gray shade due to the lack of observation. The right panel of each figure shows the logarithmic number of samples at each height. (c), (d) same to as (a) and (b) respectively, but during Case 2 (from 16 to 21 JST on August 15, 2018).